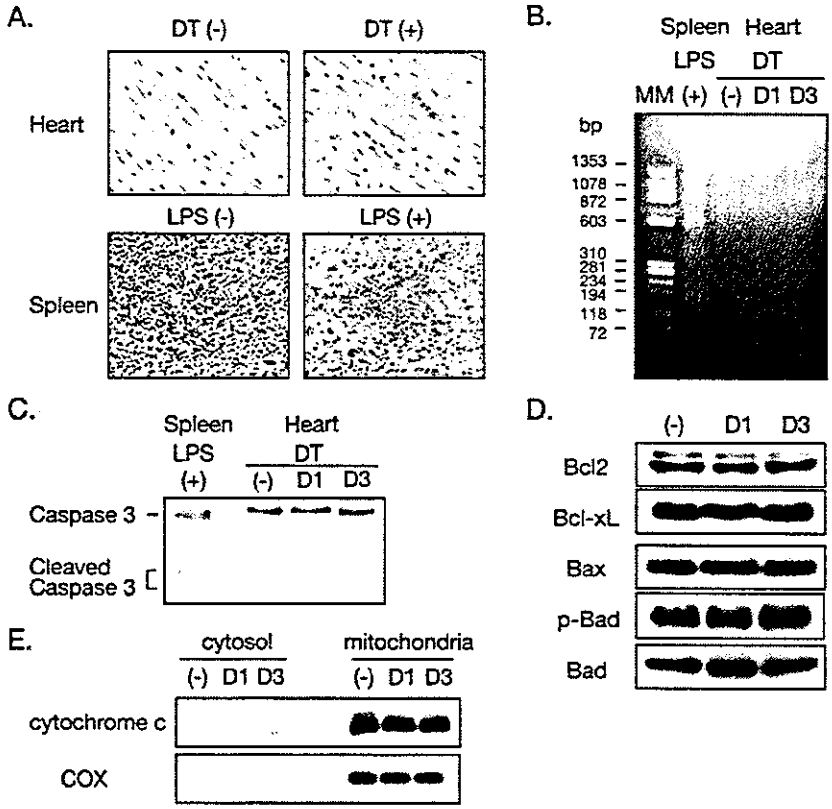

FIG. 5. **DT-induced myocardial cell death is not mediated by apoptosis, but by autophagy.** *A* and *B*, TUNEL method (*A*) and electrophoresis of genomic DNA by agarose gel (*B*) showed no evidence of DNA fragmentation in TG hearts 3 days after DT injection. Spleens from mice with lipopolysaccharide-induced sepsis were used as a positive control. *C–E*, immunoblot analysis showing no evidence of activation of caspase 3 (*C*), changes in expressions of Bcl2 family proteins (*D*) and cytochrome *c* release from mitochondria (*E*) in DT-treated TG hearts. *COX*, cytochrome *c* oxidase subunit IV. *D*, day. *LPS*, lipopolysaccharide.

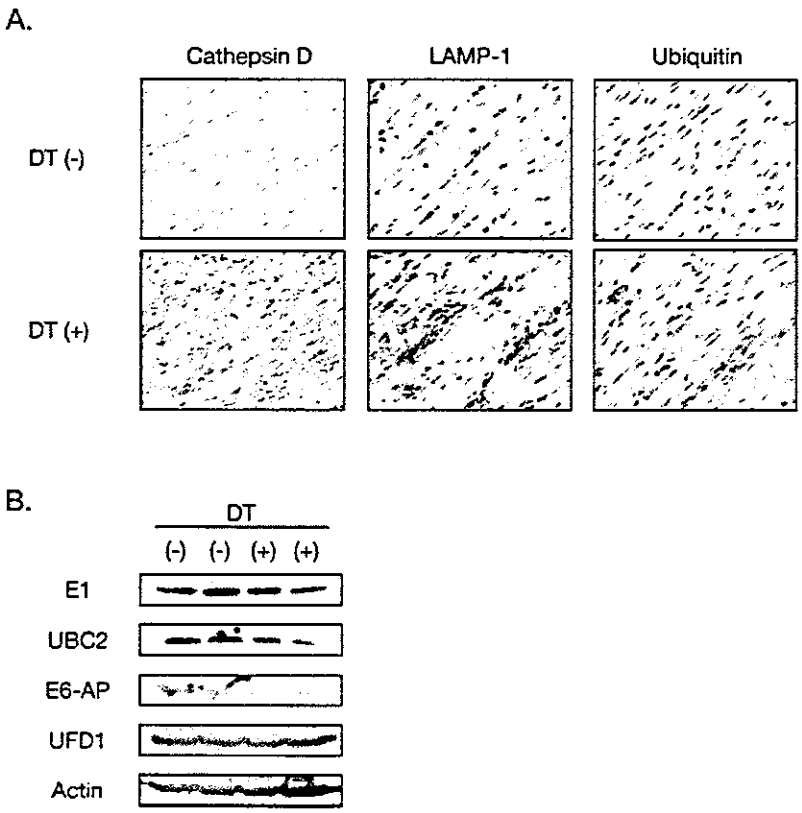

FIG. 6. **DT-induced myocardial cell death is mediated by autophagy.** *A*, immunohistochemistry showing cardiomyocytes were positively stained for cathepsin D, LAMP-1, and ubiquitin in TG hearts 3 days after DT injection. *B*, immunoblot analysis showing unchanged expression levels of the ubiquitin-activating enzyme E1, ubiquitin-conjugating enzyme E2 (*UBC2*), ubiquitin-ligating enzyme E3 (*E6-AP*), and deubiquitinating enzyme UFD1.

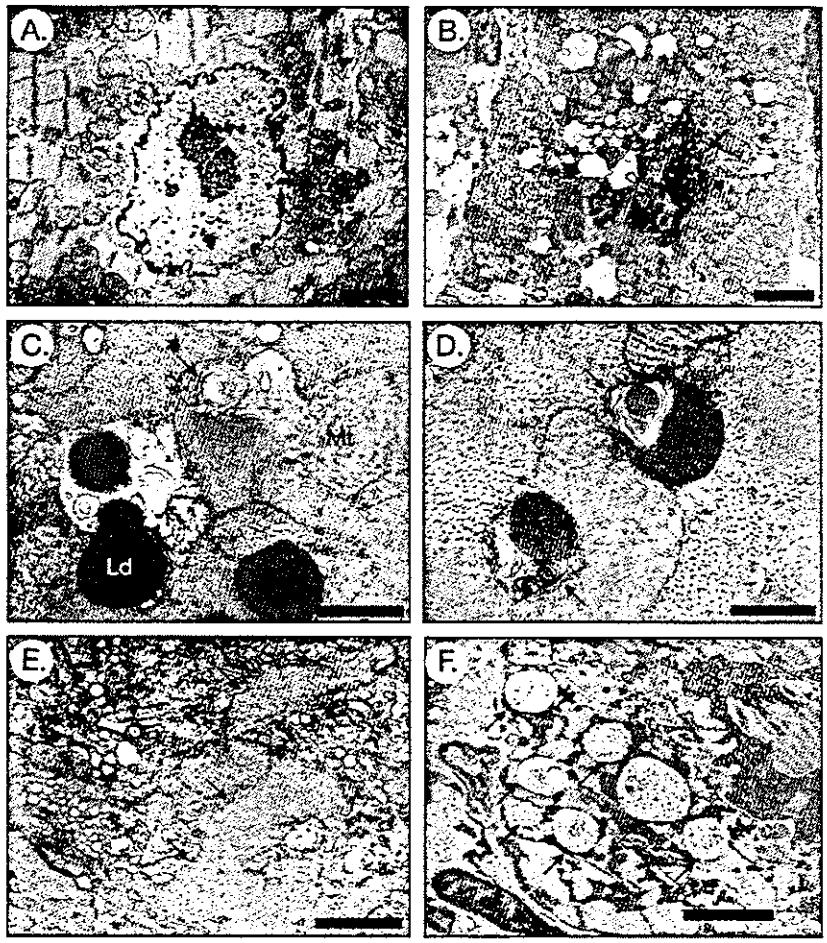

FIG. 7. **Electron microscopic analysis of the hearts after DT injection.** Electron microscopic analysis before (*A*) and after DT injection (*B–E*). In cardiomyocytes of DT-treated TG hearts, nuclear morphological changes associated with lumpy chromatin condensation were observed (*arrow* in *B*). Abundant vacuoles of various sizes in the cytoplasm (*B*) were typical autophagosomes containing degenerating lipid droplets and mitochondria (*C* and *D*). *Arrows* (in *C* and *D*) indicate myelin figures. Myofibrillar lysis (*arrows*) was observed in cardiomyocytes undergoing autophagic cell death (*E*). Electron microscopic analysis of biopsied myocardium from a patient with dilated cardiomyopathy (*F*) revealed cardiomyocytes containing many autophagosomes with degenerating mitochondria (*arrows*). *Ld*, lipid droplet; *Mt*, mitochondria. *Bars*, 2 μm (*A* and *B*), 1 μm (*C* and *E*), 0.5 μm (*D*), and 5 μm (*F*).

proteasomal proteases (21–23, 41). Consistently, elevated expressions of cathepsin D and ubiquitin were recognized in DT-treated TG cardiomyocytes (Fig. 6*A*). In contrast, biochemical signals inducing apoptosis were not activated. ACD often occurs in large, cytoplasmic-rich, and post-mitotic cells, and has been implicated in several human diseases (19, 21–23, 41). For example, ACD is associated with neurodegenerative diseases such as Parkinson's disease (42), Huntington's disease (43), and Alzheimer's disease (44). Degenerated cardiomyocytes displaying morphological features characteristic of ACD have recently been reported to exist in the failing hearts of patients with dilated cardiomyopathy, valvular heart diseases, congenital heart diseases, and hypertensive heart diseases (Fig. 7*F*) (3–7). A recent paper demonstrated that cardiomyocyte apoptosis of rare occurrence comparable with that observed in human failing hearts were sufficient to cause lethal cardiomyopathy in transgenic mice with a ligand-induced caspase-8 activation in the hearts (45). It is noteworthy that autophagic cardiomyocyte death has been reported to be detectable more frequently than apoptosis or oncosis in failing or hemodynamically overloaded human hearts (3, 6, 7), although the frequency of the each form of cell death may be influenced by disease stages and backgrounds (*e.g.* age, etiology, clinical feature, and treatment) of the examined samples (2).

Recent studies have indicated a significant role of lysosomal cysteine and aspartic protease cathepsins in execution of ACD (21, 46). PC12 cells cultured in a serum-deprived condition showed morphological features characteristic of ACD with an increase in proteolytic activity of cathepsin D (46), and forced expression of cathepsin D in PC12-induced rapid cell death, indicating a regulatory role of cathepsin D in ACD. Expression of cathepsin D was increased in DT-treated TG hearts (Fig. 6*A*). In damaged cardiomyocytes, translocation of cathepsin D from lysosomes to the cytosol was evident, which is indicative of enhanced proteolytic activity (47). Cathepsin D has been reported to be activated in human failing hearts (5) and also to be a positive mediator of apoptotic cell death (22, 47). Further experiments are required to clarify whether cathepsin D is involved in execution of myocardial ACD in the pathogenesis of heart failure and how cathepsin D regulates these modes of cell death differentially.

According to the recent studies, ubiquitin-dependent protein degradation is linked to autophagy (48). Accumulation of ubiquitin in cardiomyocytes was observed in DT-treated TG hearts (Fig. 6*A*) as well as in human failing hearts (4, 6, 7). Kostin *et al.* (6) demonstrated a functional defect in the ubiquitin/proteasome pathway together with ubiquitin accumulation in human failing hearts, and speculated that an excess of ubiquitinated proteins might activate autophagic protein degradation. The precise molecular mechanisms of how ubiquitin accumulation enhances autophagy remain unknown, although ubiquitination is postulated to be required for maturation of autophagosomes (48). Unlike human failing hearts (6), the amounts of UBC2 and UFD1 were unchanged in the hearts of our model mice (Fig. 6*B*). Protein ubiquitination and deubiquitination are mediated by a large number of enzymes (49), and it is an important issue to be

addressed in the future how ubiquitin is accumulated in cardiomyocytes undergoing autophagic cell death.

Diphtheria is a communicable disease affecting the upper respiratory tract and occasionally the skin as primary infection (50). However, remote organs such as heart or peripheral nerves are often damaged when DT is absorbed into the systemic circulation. Although diphtheria infection has been rarely encountered in developed countries because of the high rates of vaccination after the mid 1960s, several sporadic outbreaks occurred, for example, in the former Union of Soviet Socialist Republics in 1990s (50). Myocardial involvement is a major complication that determines the prognosis, but the pathophysiology associated with diphtheritic cardiomyopathy remains largely unknown. Histological analysis of the postmortal heart of a diphtheria patient revealed hyaline degeneration of myocardium and infiltration of mononuclear cells, and cytosolic lipid droplets and clumped chromatin granules were observed by electron microscopic examination (51). Although vacuoles of autophagosomes were not described in this paper, these findings were similar to those observed in our mouse model. Interestingly, cardiomyocyte loss through ACD associated with a decrease in protein synthesis was also observed in anthracycline-induced cardiomyopathy (52). Therefore, autophagic cardiomyocyte death evoked by a decrease in protein synthesis might not be confined to diphtheritic cardiomyopathy, but a more generalized phenomenon that occurs during progression of heart failure arising from miscellaneous etiologies. In this regard, our model of experimentally induced heart failure will be useful to elucidate molecular mechanisms underlying structural and functional changes associated with ACD in heart failure.

Acknowledgments—We thank R. Kobayashi, E. Fujita, and M. Iida for excellent technical assistance. We are grateful to Dr. A. Ullrich (Max-Planck-Institute of Biochemistry, Martinsried, Germany) and Dr. J. Robbins (Children's Hospital, Cincinnati, OH) for providing cDNAs.

REFERENCES

1. Nadal, G. B., Kajstura, J., Leri, A., and Anversa, P. (2003) *Circ. Res.* **92,** 139–150
2. Kang, P. M., and Izumo, S. (2000) *Circ. Res.* **86,** 1107–1113
3. Yamamoto, S., Sawada, K., Shimomura, H., Kawamura, K., and James, T. N. (2000) *J. Mol. Cell Cardiol.* **32,** 161–175
4. Knaapen, M. W., Davies, M. J., De, B. M., Haven, A. J., Martinet, W., and Kockx, M. M. (2001) *Cardiovasc. Res.* **51,** 304–312
5. Shimomura, H., Terasaki, F., Hayashi, T., Kitaura, Y., Isomura, T., and Suma, H. (2001) *Jpn. Circ. J.* **65,** 965–968
6. Kostin, S., Pool, L., Elsasser, A., Hein, S., Drexler, H. C., Arnon, E., Hayakawa, Y., Zimmermann, R., Bauer, E., Klovekorn, W. P., and Schaper, J. (2003) *Circ. Res.* **92,** 715–724
7. Hein, S., Arnon, E., Kostin, S., Schonburg, M., Elsasser, A., Polyakova, V., Bauer, E. P., Klovekorn, W. P., and Schaper, J. (2003) *Circulation* **107,** 984–991
8. Mann, D. L. (1999) *Circulation* **100,** 999–1008
9. Schaper, J., Elsasser, A., and Kostin, S. (1999) *Circ. Res.* **85,** 867–869
10. Anversa, P. (2000) *Circ. Res.* **86,** 121–124
11. Pappenheimer, A. J. (1977) *Annu. Rev. Biochem.* **46,** 69–94
12. Falnes, P. O., and Sandvig, K. (2000) *Curr. Opin. Cell Biol.* **12,** 407–413
13. Van Ness, B. G., Howard, J. B., and Bodley, J. W. (1980) *J. Biol. Chem.* **255,** 10710–10716
14. Higashiyama, S., Abraham, J. A., Miller, J., Fiddes, J. C., and Klagsbrun, M. (1991) *Science* **251,** 936–939
15. Naglich, J. G., Metherall, J. E., Russell, D. W., and Eidels, L. (1992) *Cell* **69,** 1051–1061
16. Mitamura, T., Umata, T., Nakano, F., Shishido, Y., Toyoda, T., Itai, A., Kimura, H., and Mekada, E. (1997) *J. Biol. Chem.* **272,** 27084–27090
17. Saito, M., Iwawaki, T., Taya, C., Yonekawa, H., Noda, M., Inui, Y., Mekada, E., Kimata, Y., Tsuru, A., and Kohno, K. (2001) *Nat. Biotechnol.* **19,** 746–750
18. Kim, J., and Klionsky, D. J. (2000) *Annu. Rev. Biochem.* **69,** 303–342
19. Klionsky, D. J., and Emr, S. D. (2000) *Science* **290,** 1717–1721
20. Ohsumi, Y. (2001) *Nat. Rev. Mol. Cell. Biol.* **2,** 211–216
21. Bursch, W. (2001) *Cell Death Differ.* **8,** 569–581
22. Leist, M., and Jaattela, M. (2001) *Nat. Rev. Mol. Cell. Biol.* **2,** 589–598
23. Lockshin, R. A., and Zakeri, Z. (2002) *Curr. Opin. Cell Biol.* **14,** 727–733
24. Takano, H., Nagai, T., Asakawa, M., Toyozaki, T., Oka, T., Komuro, I., Saito, T., and Masuda, Y. (2000) *Circ. Res.* **87,** 596–602
25. Asakawa, M., Takano, H., Nagai, T., Uozumi, H., Hasegawa, H., Kubota, N., Saito, T., Masuda, Y., Kadowaki, T., and Komuro, I. (2002) *Circulation* **105,** 1240–1246
26. Toko, H., Zhu, W., Takimoto, E., Shiojima, I., Hiroi, Y., Zou, Y., Oka, T., Akazawa, H., Mizukami, M., Sakamoto, M., Terasaki, F., Kitaura, Y., Takano, H., Nagai, T., Nagai, R., and Komuro, I. (2002) *J. Biol. Chem.* **277,** 24735–24743
27. Akazawa, H., Komuro, I., Sugitani, Y., Yazaki, Y., Nagai, R., and Noda, T. (2000) *Genes Cells* **5,** 499–513
28. Vander, H. M., Chandel, N. S., Williamson, E. K., Schumacker, P. T., and Thompson, C. B. (1997) *Cell* **91,** 627–637
29. Saito, S., Hiroi, Y., Zou, Y., Aikawa, R., Toko, H., Shibasaki, F., Yazaki, Y., Nagai, R., and Komuro, I. (2000) *J. Biol. Chem.* **275,** 34528–34533
30. Chau, B. N., Borges, H. L., Chen, T. T., Masselli, A., Hunton, I. C., and Wang, J. Y. (2002) *Nat. Cell Biol.* **4,** 757–765
31. Komazaki, S., Ito, K., Takeshima, H., and Nakamura, H. (2002) *FEBS Lett.* **524,** 225–229
32. Komuro, I., and Yazaki, Y. (1993) *Annu. Rev. Physiol.* **55,** 55–75
33. Sadoshima, J., and Izumo, S. (1997) *Annu. Rev. Physiol.* **59,** 551–571
34. de Lemos, J. A., McGuire, D. K., and Drazner, M. H. (2003) *Lancet* **362,** 316–322
35. Mercadier, J. J., Lompre, A. M., Duc, P., Boheler, K. R., Fraysse, J. B., Wisnewsky, C., Allen, P. D., Komajda, M., and Schwartz, K. (1990) *J. Clin. Investig.* **85,** 305–309
36. Elsner, D., and Riegger, G. A. (1995) *Curr. Opin. Cardiol.* **10,** 253–259
37. Arber, S., Hunter, J. J., Ross, J. J., Hongo, M., Sansig, G., Borg, J., Perriard, J. C., Chien, K. R., and Caroni, P. (1997) *Cell* **88,** 393–403
38. Sussman, M. A., Welch, S., Cambon, N., Klevitsky, R., Hewett, T. E., Price, R., Witt, S. A., and Kimball, T. R. (1998) *J. Clin. Investig.* **101,** 51–61
39. Lee, P., Morley, G., Huang, Q., Fischer, A., Seiler, S., Horner, J. W., Factor, S., Vaidya, D., Jalife, J., and Fishman, G. I. (1998) *Proc. Natl. Acad. Sci. U. S. A.* **95,** 11371–11376
40. Anversa, P., Zhang, X., Li, P., and Capasso, J. (1992) *J. Clin. Investig.* **89,** 618–629
41. Lockshin, R. A., Osborne, B., and Zakeri, Z. (2000) *Cell Death Differ.* **7,** 2–7
42. Anglade, P., Vyas, S., Javoy-Agid, F., Herrero, M. T., Michel, P. P., Marquez, J., Mouatt-Prigent, A., Ruberg, M., Hirsch, E. C., and Agid, Y. (1997) *Histol. Histopathol.* **12,** 25–31
43. Kegel, K. B., Kim, M., Sapp, E., McIntyre, C., Castano, J. G., Aronin, N., and DiFiglia, M. (2000) *J. Neurosci.* **20,** 7268–7278
44. Cataldo, A. M., Hamilton, D. J., Barnett, J. L., Paskevich, P. A., and Nixon, R. A. (1996) *J. Neurosci.* **16,** 186–199
45. Wencker, D., Chandra, M., Nguyen, K., Miao, W., Garantziotis, S., Factor, S. M., Shirani, J., Armstrong, R. C., and Kitsis, R. N. (2003) *J. Clin. Investig.* **111,** 1497–1504
46. Uchiyama, Y. (2001) *Arch. Histol. Cytol.* **64,** 233–246
47. Roberg, K., and Ollinger, K. (1998) *Am. J. Pathol.* **152,** 1151–1156
48. Blommaart, E. F., Luiken, J. J., and Meijer, A. J. (1997) *Histochem. J.* **29,** 365–385
49. Pickart, C. M. (2004) *Cell* **116,** 181–190
50. Hadfield, T. L., McEvoy, P., Polotsky, Y., Tzinserling, V. A., and Yakovlev, A. A. (2000) *J. Infect. Dis.* **181,** Suppl. 1, S116–S120
51. Burch, G. E., Sun, S. C., Sohal, R. S., Chu, K. C., and Colcolough, H. L. (1968) *Am. J. Cardiol.* **21,** 261–268
52. Semenov, D. E., Lushnikova, E. L., and Nepomnyashchikh, L. M. (2001) *Bull. Exp. Biol. Med.* **131,** 505–510

Circ J 2004; **68:** 769–777

New Method of Measuring Coronary Diameter by Electron-Beam Computed Tomographic Angiography Using Adjusted Thresholds Determined by Calibration With Aortic Opacity

Nobusada Funabashi, MD; Yoshiki Kobayashi, MD*; Masayuki Kudo, RT**; Miki Asano, MT; Kiyomi Teramoto, MD; Issei Komuro, MD; Geoffrey D Rubin, MD†

Background In a previous study the adjusted thresholds at which the diameters of coronary arteries determined by enhanced electron-beam computed tomography (CT) scans are equal to the corresponding quantitative coronary angiography measurements were analyzed, and their correlation with maximum CT values for the vessel short axes was determined. A rapid accurate method for such measurements was sought by substituting maximum CT values for the descending aorta in the corresponding axial images for those for the short axes.
Methods and Results In 8 patients, 179 sites were measured. Means (±SD) of adjusted thresholds and the maximum CT values for vessel short axes and the descending aorta in the corresponding axial images for all vessels were 108±66, 227±80, and 363±75 Hounsfield Unit (HU), respectively. Adjusted thresholds correlated with the maximum CT values for the corresponding vessel short axes and the descending aorta in the corresponding axial images, with R^2=0.55, 0.33, $p<0.01$, respectively. An abbreviated formula for use of maximum CT values for the descending aorta in the corresponding axial images was y=0.5x–75 (HU) (y=adjusted threshold, x=maximum CT value for the descending aorta in the corresponding axial image).
Conclusions The abbreviated formula provided a rapid, accurate method for measurements independent of arterial enhancement. (*Circ J* 2004; **68:** 769–777)

Key Words: Adjusted thresholds; Coronary artery; Electron beam computed tomography; Quantitative coronary angiography

Measurements of the diameters of 3-dimensional (3-D) coronary arteries using electron-beam computed tomography (EBCT) and shaded surface display (SSD) techniques have been qualitatively compared with those obtained by cine coronary angiography[1–3] The threshold selection has been set at 80–100 Hounsfield Units (HU) and from quantitative analysis using different threshold selections[4] it is reasonable to expect that the optimal threshold level for SSD depends on the magnitude of arterial enhancement. As a result, we hypothesized that a single threshold setting would not constitute a reliable measurement of coronary arterial luminal diameter using EBCT. We have previously reported that adjusted threshold methods using line density profile (LDP) curves in consideration of arterial enhancement provided more accurate results than fixed threshold methods[5,6] However, in routine practice it is unrealistic to make an LDP curve, or to measure the maximum computed tomography (CT) value for the short axis at each site in the coronary arteries.

In the present study, we analyzed the adjusted thresholds at which the diameters of coronary arteries determined by EBCT scans are equal to the corresponding quantitative coronary angiography (QCA) measurements. Calibration using aortic opacity of the opacified blood, and using maximum CT values for the descending aorta in the corresponding axial images as a substitute for the maximum CT values for the short axes of the coronary arteries, was performed to accurately resolve the measurements of coronary artery luminal diameter. Furthermore we sought to establish a simplified method for measuring coronary artery diameters that was independent of inter- and intra-patient variations in arterial enhancement.

Methods

Patients

Under a protocol approved by the institutional committee for the protection of human subjects and after informed consent was obtained, 8 male patients aged 53–63 years old, who had previously undergone heart transplantation at a mean 3.6 years prior to enrollment, were recruited to undergo both EBCT (Imatron C-150XP, Imatron, South San Francisco, CA, USA) and cine coronary angiography within a 24-h period.

(Received February 24, 2004; revised manuscript received May 13, 2004; accepted May 28, 2004)
*Department of Cardiovascular Science and Medicine, Chiba University Graduate School of Medicine, Chiba, *First Department of Internal Medicine, Osaka City University, Osaka, **GE Yokokawa Medical Systems, Tokyo and †Department of Radiology, Stanford University School of Medicine, California, USA*
Mailing address: Nobusada Funabashi, MD, Department of Cardiovascular Science and Medicine, Chiba University Graduate School of Medicine, 1-8-1 Inohana, Chuo-ku, Chiba, Chiba 260-8670, Japan. E-mail: nobusada@ma.kcom.ne.jp

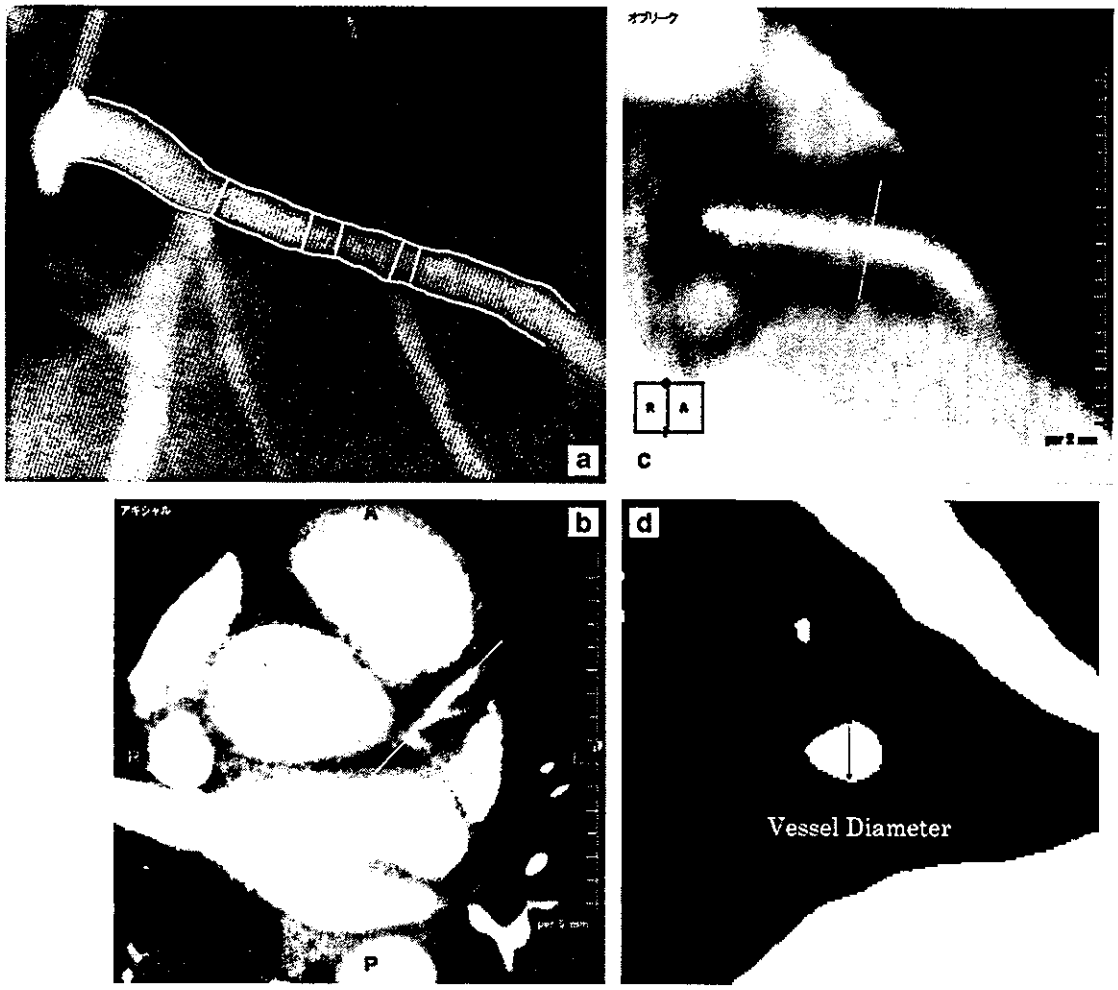

Fig 1. (a) Quantitative coronary angiogram showing the 30-degree right anterior oblique projection of the left coronary arteries. Lines indicate manual tracing. (b–d) Schema of measurement of adjusted thresholds using electron-beam computed tomography (CT). (b) Transverse source image obtained with contrast-enhanced electron-beam CT. The yellow line indicates the long axis of the LAD branch with which we measured vessel diameters. (c) Oblique planar image parallel to the long axis of the LAD branch. The yellow line indicates the axis perpendicular to the long axis of the vessel. Diameters were measured perpendicular to the median centerline of the vessel. Oblique planar reformations were generated parallel to the long axis of vessel, which approximates the oblique projections analyzed with cine coronary angiography. (d) Oblique planar image perpendicular to the long axis of the LAD branch. By setting the display width at zero, we were able to reduce the grayscale to black and white. We set the window levels at the site at which the vessel diameters were equal to the diameters measured by quantitative coronary angiography (QCA) measurement; these window levels were regarded as the adjusted thresholds. Vessel diameters were measured at each measurement site in the same direction as for the coronary angiograms.

Cine Coronary Angiography

Cine coronary angiography was performed using the percutaneous femoral approach. Sublingual nitroglycerin (0.4 mg) was given 2–3 min before the contrast injection, to minimize the effect of varying vasomotor tone on vessel lumen diameters. Catheters of known diameters were used for calibration. Multiple projections, including cranial and caudal angulated views, were obtained for all patients. The 30-degree right anterior oblique (RAO) projection was used to assess the left coronary artery (LCA) and its branches, and the 60-degree left anterior oblique (LAO) projection was used to assess the right coronary artery (RCA).

QCA was performed off-line using a computerized edge detection program (QCA plus, Sanders Data System, Palo Alto, CA, USA) developed and validated at Stanford[7] and analyzed by a cardiologist (Y.K.) unaware of the EBCT results (Fig 1a). Diameters of the proximal left main (LM) artery and its distal end just above the bifurcation of the left anterior descending branch (LAD) and the left circumflex branch (LCX) were recorded, as well as the diameter at a point between these 2 sites. Also measured were the diameters of the LAD, the LCX, and the RCA, each at their proximal ends and at 2–4 equally spaced points between their proximal ends and the first atrial side branch. Single end-diastolic cine frames, identified by an electrocardiogram-triggered mark on the frames and selected for optimal coronary vessel opacification, were focused and magnified. The digitized image was displayed on a graphic computer terminal linked to a light pen, which was used to manually trace the margins of either the catheter or coronary segment. Using these lines as initial search locations, the automatic edge-finding algorithm drew and smoothed the edges, defining the edge as the peak of the first derivative of the gray-scale density gradient, perpendicular to the long axis

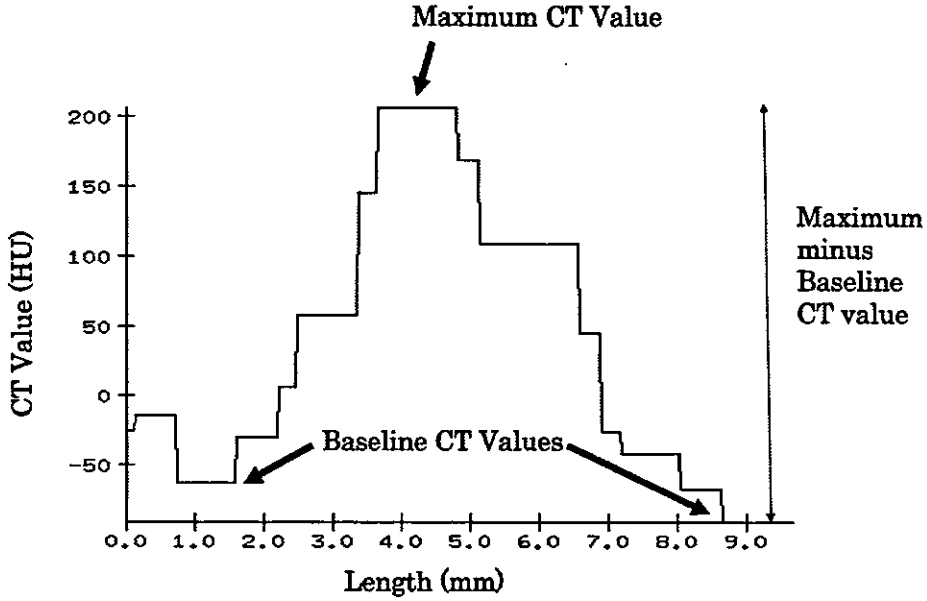

Fig 2. Schema of line density profile (LDP) method. Plot shows the voxel values along a line that is perpendicular to the median centerline of the vessel at each measurement site. In this schema, the baselines of the LDP were established as the epicardial fat immediately adjacent to the vessel on both sides. For the LDP curve, baseline computed tomography (CT) values were calculated for the right side and the left side in addition to the maximum CT value represented as the schema. We measured the maximum CT value minus baseline CT value at both sides and used both the larger and average values.

of the catheter or vessel, as estimated from the initial manual tracings. When the computer algorithm was unable to resolve vessel boundaries in areas of noise or vessel crossings, manual editing of short segments of boundary with the light pen was used to correct the computer-generated boundary. At no time did the length of a manually entered margin exceed 20% of the total length of the quantitated segment. After the light pen indicated the start and end of the segment, the mean diameter of the segment was computed from perpendiculars constructed through the length of a computer-generated centerline. The distance of each measurement point from the LM or the RCA ostium was measured.

EBCT Measurement

EBCT attains ultrafast scan speeds by sweeping a steered electron beam on a fixed tungsten target ring, thereby providing a moving X-ray source without mechanical motion[8] The 100-ms modes are used for high-resolution cross-section imaging in a Step-Volume Scan mode with electrocardiogram gating[9] EBCT was coupled to a 160 ml intravenous injection of iodinated contrast material (300 mg/ml) performed during breath holding, and was directed over 60–70 mm of the proximal and middle portions of the coronary arteries using 1.5 mm collimation, 1.0 mm table incrementation, and triggered to 80% of the R-to-R interval. The patients received nitroglycerin prior to EBCT, as in the cine angiography studies.

EBCT data were transferred to a workstation (Advantage-Windows, General Electronics, Milwaukee, WI, USA) and 18–27 measurement points per patient within the coronary tree were defined relative to identifiable branches.

Vessel diameters were measured at each measurement site in the same direction as the QCA measurements. Diameters were analyzed by a cardiologist (N.F.) unaware of the QCA results, using the workstation program described later (Fig 1 b–d). Double oblique planar reformations were generated, firstly parallel to the long axes of the vessels, approximating the oblique projections analyzed by cine coronary angiography (Fig 1 b,c). Using the vessel origins and the major branch sites as landmarks, the loci corresponding to the QCA measurement were identified on the EBCT scans. Second, an additional oblique planar reformation was generated perpendicular to the first oblique reformation image (long axes of the vessel) (Fig 1c). By setting the display width at zero, we were able to reduce the grayscale to black and white (Fig 1d). We set the window levels at the site at which vessel diameters were equal to the diameters obtained by QCA measurement; these window levels were regarded as the adjusted thresholds. Furthermore, LDP curves were made perpendicular to the median centerline of the vessel at each measurement site. A plot of the voxel values along a line perpendicular to the vessel at each measurement site was created (Fig 2). The baseline of the LDP was established as epicardial fat or myocardium immediately adjacent to the artery. For the LDP curve, baseline CT values were calculated for the right and left sides in addition to the maximum CT value. We measured the maximum CT value minus baseline CT value using the larger and average values for both sides in the scatter plot. The maximum CT value for the short axis of the coronary arterial lumen at each measurement site was measured from the oblique planar reformations perpendicular to the long axis of the vessel. Also, the maximum CT value for the descending aorta at the corresponding axial level of each measurement site was measured. As some calcifications, which apparently caused a higher attenuation than the vessel lumen, were evident on the enhanced axial images of the descending aorta, we carefully excluded them and measured the maximum CT values for the descending aorta. The maximum CT value was used as an index for assessing arterial enhancement.

Table 1 QCA Diameter With Distance From the Ostium

Vessel type	n	QCA Diameter (mm)	Distance from Ostium (mm)
LM	11	5.07±0.75 (3.82–6.09)	3.21±2.9 (0–9.39)
LAD	62	3.3±0.85 (1.46–5.28)	34.64±17.13 (5–77.64)
LCX	46	3.53±0.76 (1.52–5.27)	23.81±15.16 (3–62.54)
RCA	60	3.61±0.58 (2.71–5.67)	28.56±20.93 (0–79.77)
Total	179	3.57±0.84 (1.46–6.09)	27.89±19.04 (0–79.77)

QCA, quantitative coronary arterigraphy; LM, left main; LAD, left anterior descending branch; LCX, left circumflex branch; RCA, right coronary artery.

Table 2 QCA Diameter, Distance From the Ositum, Adjusted Threshold, and Maximum CT Values for Each Patient

Patient no.	n	QCA Diameter (mm)	Distance from ostium (mm)	Adjusted threshold (HU)	Maximum CT value in short axis (HU)	Maximum CT value in aorta (HU)
1	18	3.31±1.19	22.2±16.3	138±44	214±37	344±28
2	23	3.25±0.73	25.9±17.4	80±35	169±57	293±22
3	20	4.06±0.9	20.1±17.6	148±32	282±33	376±31
4	20	3.57±0.46	25.2±16.6	85±46	210±37	374±14
5	26	3.57±0.69	30.2±16.9	196±41	327±92	475±40
6	24	3.57±0.56	32.5±21.4	69±39	243±65	412±25
7	21	3.57±0.48	26.1±15.7	110±59	213±56	349±27
8	27	3.57±0.64	36.2±21.8	48±59	155±43	276±76
Total	179	3.57±0.84	27.9±19	108±66	227±80	363±75

QCA, quantutative coronary arteriography; HU, Hounsfield Units.

Table 3 QCA Diameter, Distance From the Ostium, Adjusted Threshold, and Maximum CT Values for Each Vessel

Vessel site	n	QCA diameter (mm)	Distance from ostium (mm)	Adjusted threshold (HU)	Maximum CT value in short axis (HU)	Maximum CT value in aorta (HU)
LM	11	5.07±0.72	3.2±2.8	112±42	263±71	349±49
LAD	62	3.3±0.84	34.6±17	107±69	207±71	338±82
<30 mm from ostium	25	3.88±0.74	18.7±7.4	79±64	204±71	337±78
≥30 mm from ostium	37	2.92±0.67	45.4±12.6	127±65	209±72	339±86
LCX	46	3.53±0.75	23.8±15	85±55	203±52	368±63
<30 mm from ostium	30	3.66±0.74	14.3±6.5	80±49	208±46	355±62
≥30 mm from ostium	16	3.29±0.72	41.6±9	94±63	192±61	393±58
RCA	60	3.61±0.57	28.6±20.8	126±70	259±93	387±69
<30 mm from ostium	31	3.81±0.61	11.6±9.3	118±78	256±93	371±67
≥30 mm from ostium	29	3.4±0.44	46.7±12.7	135±59	262±92	404±68
Total	179	3.57±0.84	27.9±19	108±66	227±80	363±75

QCA, quantitative coronary arteriography; LM, left main; LAD, left anterior descending branch; LCX, left circumflex branch; RCA, right coronary artery; HU, Hounsfield Units.

Statistical Analysis

Adjusted thresholds were correlated with arterial enhancement (maximum CT values for the vessel short axes, the descending aorta in the corresponding axial images, vessel sizes (the corresponding QCA diameter measurements), and the distances from the vessel ostium. Variations between the 2 groups (adjusted thresholds and thresholds according to the abbreviated formula) were compared using the F distribution test.

Results

QCA Diameters With Distances From the Ostium

All 8 cine coronary angiograms were interpreted as being normal. A total of 179 sites were measured among the 8 patients (LM, 11; LAD, 62; LCX, 46; RCA, 60).

Table 1 lists the QCA diameters with the distances from the LM or RCA ostium. The QCA diameters ranged from 1.46 mm to 6.09 mm (mean ± SD, 3.57±0.84 mm). Distances from the ostium ranged from 0 to 79.77 mm (27.9± 19.04 mm).

EBCT Measurement With Arterial Enhancement

Table 2 lists the number of vessel sites, QCA diameters (mean ± SD), distances from the ostium, adjusted thresholds, and maximum CT values for the vessel short axes and the descending aorta in the corresponding axial images for each patient.

Table 3 lists the number of vessel sites, distances from the ostium (mean ± SD), adjusted thresholds and maximum CT values for the vessel short axes and the descending aorta in the corresponding axial images for each vessel type. Values were further stratified according to the position of measurement from the vessel ostium. Adjusted thresholds, maximum CT values for vessel short axes and maximum CT values for the descending aorta in the corresponding axial images for all vessels were 108±66, 227± 80, and 363±75 HU, respectively.

All sites corresponding to the maximum CT values for both the vessel short axes and the descending aorta in the corresponding axial images were located approximately at the center of the vessel lumen. After review of the cine coronary angiograms and the enhanced axial images of the

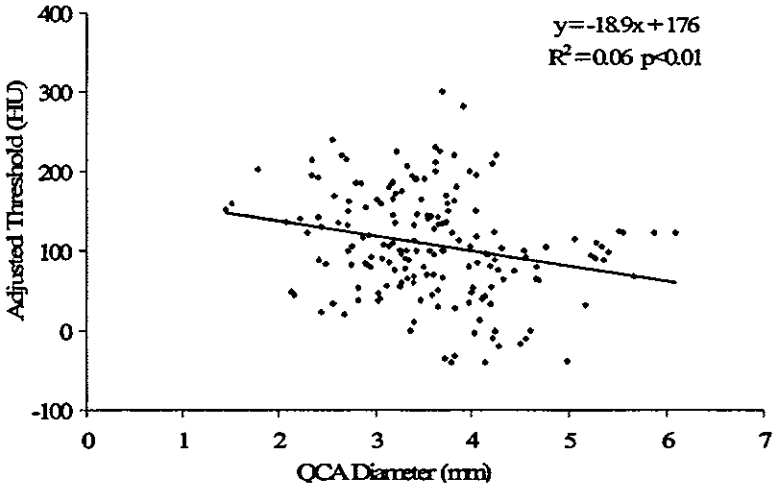

Fig3. Scatter plot of adjusted threshold vs quantitative coronary angiography (QCA) diameter. The adjusted thresholds very weakly correlated with the QCA diameters (R^2=0.06, p<0.01). These mean values were distributed about a straight line given by y=18.9x-176.

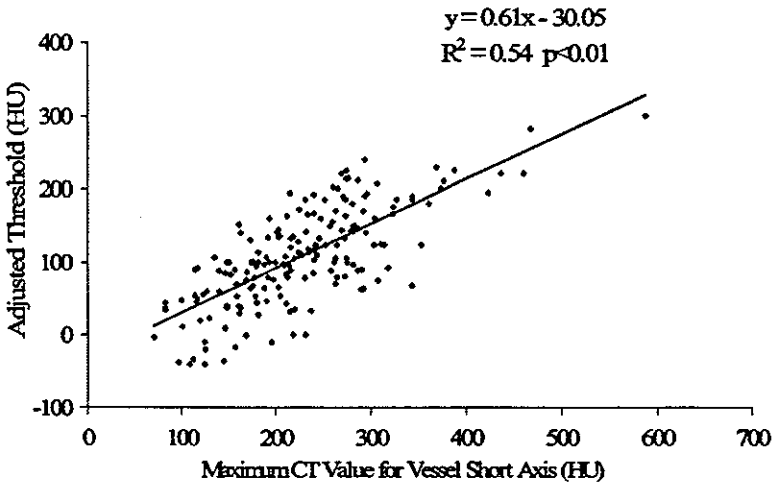

Fig4. Scatter plot of adjusted threshold vs maximum computed tomography (CT) value for the corresponding vessel short axis. The adjusted thresholds correlated with the maximum CT values for the corresponding vessel short axes (R^2=0.54, p<0.01).

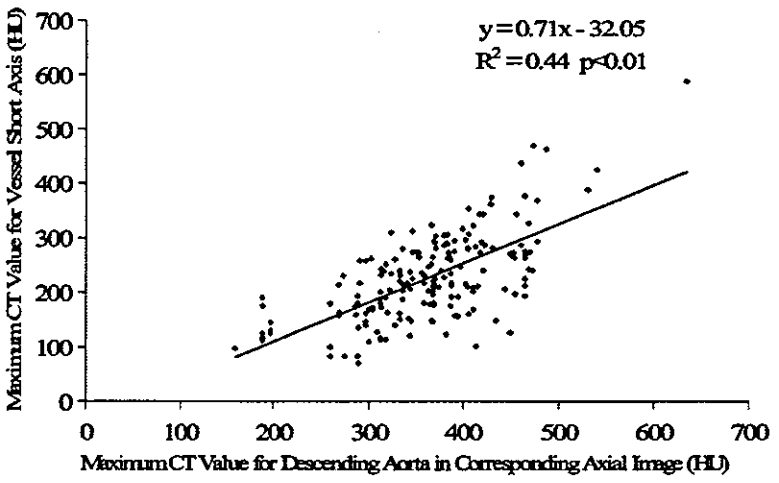

Fig5. Scatter plot of maximum computed tomography (CT) value for the vessel short axis with maximum CT value for the descending aorta in the corresponding axial image. The maximum CT values for the vessel short axes correlated with those for the descending aorta in the corresponding axial images (R^2=0.44, p<0.01). These mean values were distributed about a straight line given by y=0.71x-32.1.

EBCT data sets, we concluded that the possibility of the presence of calcification or artifact in the coronary arteries might be low; nevertheless, we were careful not to adopt the CT values relating to calcification when calculating maximum CT values for the descending aorta.

As shown in Fig3, the adjusted thresholds correlated very weakly with QCA diameters, with R^2=0.06, p<0.01. These mean values were distributed about a straight line given by y=-18.9x+176.

The adjusted thresholds correlated with maximum CT values for the corresponding vessel short axes, with R^2= 0.54, p<0.01 (Fig4). These mean values were distributed about a straight line given by y=0.61x-30.1. As shown in Fig5, the maximum CT values for the vessel short axes correlated with those for the descending aorta in the corresponding axial images with R^2=0.44, p<0.01. These mean

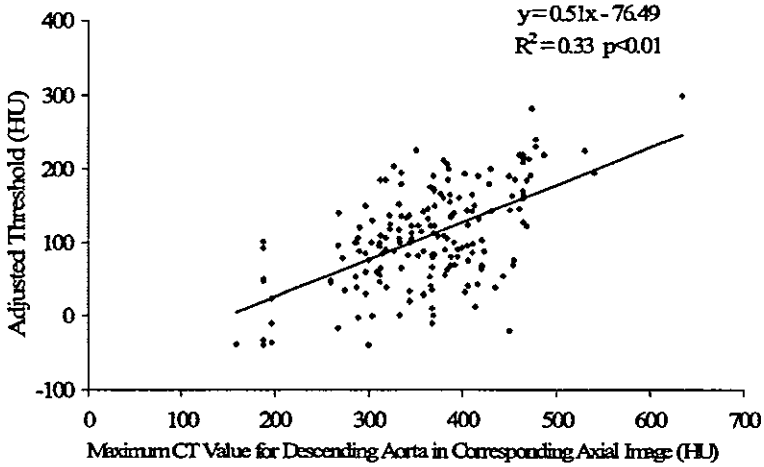

Fig 6. Scatter plot of adjusted threshold with maximum computed tomography (CT) value for the descending aorta in the corresponding axial image. The adjusted thresholds correlated with the maximum CT values for the descending aorta in the corresponding axial images (R^2=0.33, p<0.01). These mean values were distributed about a straight line given by y=0.51x−76.5. The slope of the adjusted thresholds vs the maximum CT values for the descending aorta in the corresponding axial images was approximately 0.5. The intercept of this line was −76.5 HU.

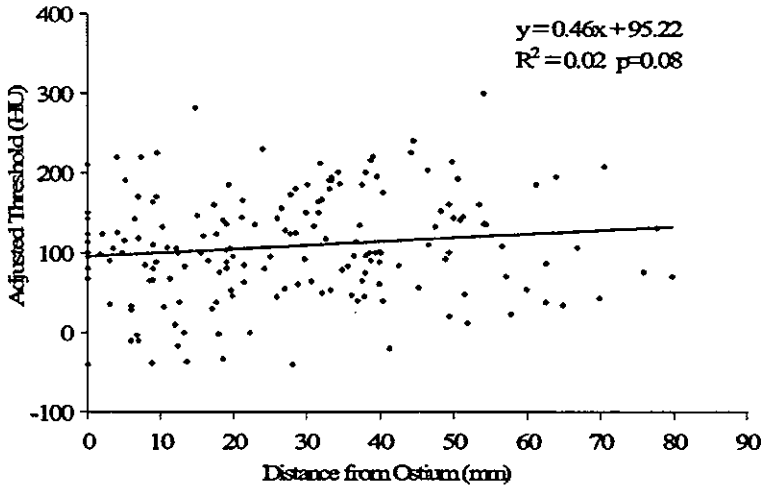

Fig 7. Scatter plot of adjusted threshold vs distance from the ostium. The adjusted thresholds did not correlate significantly with distances from the ostium (R^2=0.02, p=0.08).

values were distributed about a straight line given by y=0.71x−32.1.

The adjusted thresholds correlated with the maximum CT values for the descending aorta in the corresponding axial images with R^2=0.33, p<0.01 (Fig 6). These mean values were distributed about a straight line given by y=0.51x−76.5. The slope of the adjusted thresholds vs the maximum CT values for the descending aorta in the corresponding axial images was approximately 0.5. The intercept of this line was −76.5 HU.

As shown in Fig 7, the thresholds did not correlate significantly with distances from the ostium, with R^2=0.02, p=0.08.

As shown in Fig 8a, the adjusted thresholds correlated with the maximum minus the baseline CT values in the LDP (average of the 2 sides), with R^2=0.30, p<0.01. These mean values were distributed about a straight line given by y=0.43x−15.8. As shown in Fig 8b, the adjusted thresholds correlated with the maximum minus the baseline CT values in the LDP (larger of the 2 sides), with R^2=0.37, p<0.01. These mean values were distributed about a straight line given by y=0.47x−40.4.

From the straight line given by y=0.51x−76.5 in Fig 6, (y=adjusted threshold, x=maximum CT value for the descending aorta in the corresponding axial images), we determined the thresholds according to the abbreviated formula whereby y=0.5x−75 (HU) (y=adjusted threshold, x=maximum CT value for the descending aorta in the corresponding axial image). The constant, −75 HU, may reflect a complex of various baseline (or background) factors such as epicardial fat or myocardium. The mean (±SD) baseline CT values of the LDP of the total, the group considered to be epicardial fat and the group considered to be myocardium, were −61.0±60.4, −82.5±38.6, and 41.6±35.3 HU with ranges of −181 to 150, −181 to −2, and 0 to 150 HU, respectively.

As shown in Fig 9, the adjusted thresholds correlated with the thresholds determined by the abbreviated formula, with R^2=0.33 p<0.01. These mean values were distributed about a straight line given by y=1.02x−0.4. The slope of the adjusted thresholds vs the thresholds according to the abbreviated formula was approximately 1.0, and the intercept of this line was only −0.4 HU. In addition, the mean±SD of thresholds by the abbreviated formula was 107±37 HU. In comparing the mean±SD of the adjusted thresholds, the mean of the thresholds by the abbreviated formula was similar (107 vs 108 HU), but the standard deviation was significantly smaller (37 vs 66 HU).

As shown in Fig 10, the CT angiography diameter correlated with QCA diameter (R^2=0.09 p<0.01). The mean values were distributed about a straight line given by y=0.50x+1.86.

Discussion

Cine coronary angiography has been the standard for

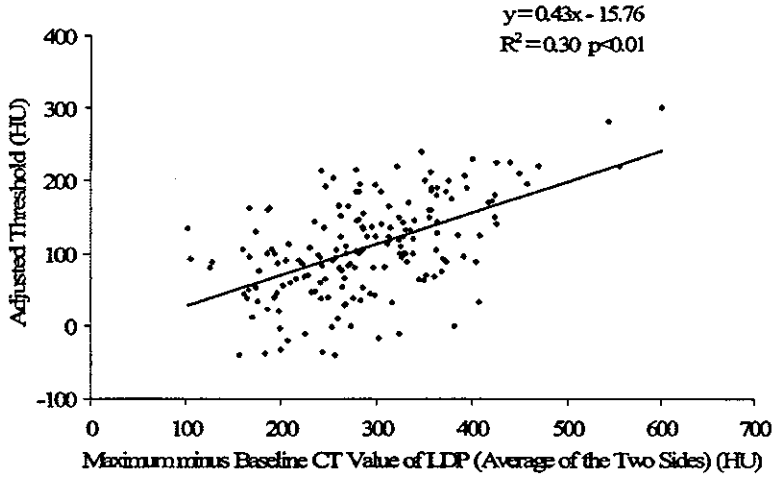

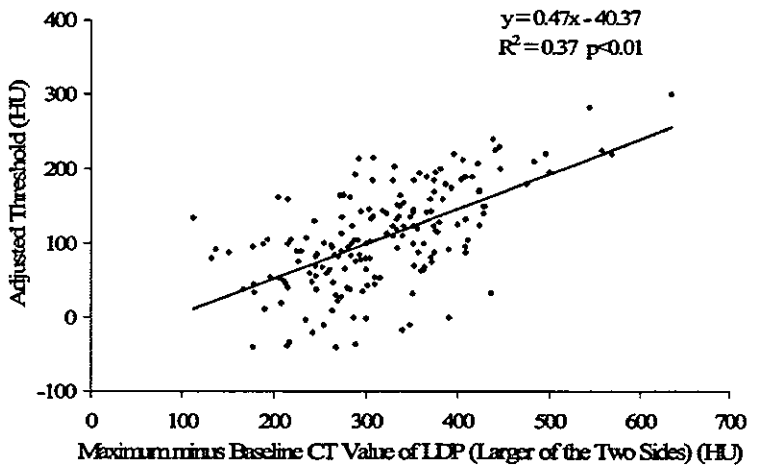

Fig 8. Scatter plots of adjusted threshold vs maximum minus the baseline computed tomography (CT) value in the line density profile (LDP) ((a) average of the 2 sides) and ((b) larger of the 2 sides). In (a) and (b), the adjusted thresholds were correlated with the maximum minus baseline CT values in the LDP (R^2=0.30, p<0.01 and R^2=0.37, p<0.01, respectively). LDP indicates line density profile.

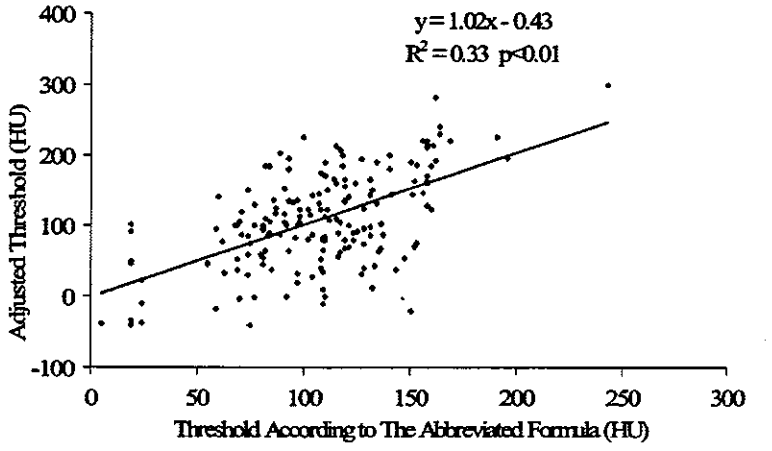

Fig 9. Scatter plot of adjusted threshold vs threshold obtained by an abbreviated formula. The adjusted thresholds correlated with threshold according to the formula (R^2=0.33, p<0.01). The mean values were distributed about a straight line given by y=1.02x–0.4. The slope of the line was approximately 1.0 and the intercept was –0.4 HU.

evaluating the extent of coronary artery disease, but recently 3-D visualization of coronary arteries using EBCT has emerged as a potential non-invasive alternative[1,2,10] Although qualitative reports have been published regarding the utility of EBCT coronary angiography[1,1–13] there are few reports of quantitative analysis of EBCT coronary angiography as compared with cine coronary angiography[5,6] We have speculated that several factors may influence the absolute luminal caliber of coronary arteries on EBCT angiograms, such as arterial enhancement, vessel diameter, distance from the ostium, and vessel types triggered to contract at the end of diastole[6]

Because the acquisition time requires 40–80 heartbeats, there must be significant differences in the state of the enhancement at the level of each slice[14] We first made a short-axis image of the coronary arteries at each site and measured the adjusted threshold at which vessel diameter was equal to that obtained from the corresponding QCA measurement.

Even though the total mean of the adjusted threshold was 108 HU, we concluded that a single threshold setting could not be used reliably to measure the luminal diameter

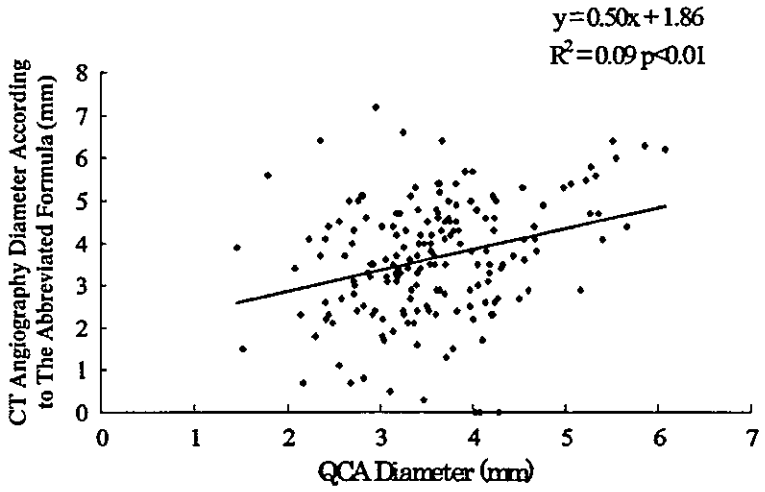

Fig 10. Scatter plot of computed tomography (CT) angiography diameter according to the abbreviated formula (mm) vs quantitative coronary angiography (QCA) diameter (mm). The CT angiography diameter according to the abbreviated formula (mm) correlated with QCA diameter (R^2=0.09 $p<0.01$). The mean values were distributed about a straight line given by y=0.50x+1.86.

of the coronary arterial tree with EBCT. However, it is unrealistic to make an LDP curve or measure the maximum CT value for the short axis at each site of the coronary arteries in routine practice. Therefore, another, easier method was needed. For this, we focused on the maximum CT values for the descending aorta in the corresponding axial images. In theory, it would be better to use the maximum minus baseline CT values than the maximum CT values alone. Therefore, we also considered the correlation between the values of R^2=0.30 for the average of the 2 sides and 0.37 for the larger of the 2 sides. Those values adjusted the thresholds with the maximum minus baseline CT values in the LDP, which gave less than the maximum CT values alone for the short axes.

To use the maximum CT values for the descending aorta in the corresponding axial images, we applied the abbreviated formula y=0.5x–75 from the straight line given by y=0.51x–76.5 (y=adjusted threshold, x=maximum CT value for the descending aorta in the corresponding axial image). If our abbreviated formula, y=0.5x–75, is to be adopted, it is necessary to measure the maximum CT values for the descending aorta in the corresponding axial images. By including the maximum intensity projection technique, it may be easy to measure the maximum CT values for the descending aorta at each axial image level and acquire information about arterial enhancement for every slice.

The adjusted thresholds correlated with the thresholds obtained from the abbreviated formula, with R^2=0.33, and the mean values were distributed about a straight line given by y=1.02x–0.4. The slope of the adjusted thresholds vs the thresholds according to the abbreviated formula was approximately 1.0, and the intercept of this line was only –0.4 HU. In comparing the thresholds according to the abbreviated formula with the adjusted thresholds, the means were similar but the standard deviation was significantly smaller in the thresholds obtained from the abbreviated formula. Therefore, adoption of the thresholds by the abbreviated formula makes it possible to achieve accurate measurements for the evaluation of coronary arteries.

In the scatter plot of the adjusted threshold vs the QCA diameter (Fig 3), the smaller the vessel diameter, the greater the adjusted threshold. Achenbach et al reported that when using 100 HU as the fixed lower threshold, they tended to underestimate small vessel diameters by the partial volume effect.[15] We obtained the opposite result and we speculate that this phenomenon might also be caused by other factors such as vessel type, arterial enhancement, vessel orientation, etc. For example, as shown in Table 3, the mean of the adjusted threshold for the portions of the RCA that were 30 mm or more from the ostium was 135 HU, whereas that of the portions of LCX at 30 mm or more from the ostium was 94 HU. Thus, when we adopted 100 HU as the fixed lower threshold, we overestimated the diameters of the portion of RCA that were 30 mm or more from the ostium, but underestimated those of the portion of the LCX that were 30 mm or more from the ostium. The adjusted thresholds correlated very weakly, or non-significantly, to the corresponding diameters measured by QCA, or the distances from the ostium, respectively.

Recently, 16-detector row multislice computed tomography (MSCT)[16,17] has become available and takes less than 25 s to image the whole heart, even if a slice thickness less than 1 mm is selected; this time interval is approximately half to one-third that required for EBCT. Therefore with MSCT, differences in the degree of arterial enhancement would influence the quality of the coronary arterial images to a lesser extent than with EBCT. Some investigators have tried to keep the same degree of arterial enhancement by improving the method of injection of the contrast material, for example via the biphase injection protocol.[18] If the MSCT coronary angiogram replaced the conventional coronary angiogram only for evaluation of the coronary arterial lumen, the calibration with aortic opacity of the opacified blood would improve the quantitative accuracy of the vessel diameters. Further studies using up-to-date MSCT and EBCT are needed to quantitatively compare the coronary artery diameters with those from QCA.

Although EBCT has worse spatial resolution than MSCT, especially in the through-plane, EBCT delivers a much lower radiation dose than MSCT, so it is still an important diagnostic modality, especially for healthy subjects.

Conclusion

We measured the adjusted thresholds at which the coronary arterial diameters on EBCT scans were equal to those obtained by a QCA measurement program. We classified a total of 179 sites among 8 patients and 4 vessel types, and further stratified measurements according to positions in relation to the vessel ostium. The means of the adjusted thresholds changed from patient to patient and from vessel

to vessel.

The adjusted thresholds correlated only very weakly, or non-significantly, with the corresponding QCA measurement diameters, or with the distances from the ostium. However, there was a correlation with maximum CT values for the vessel short axes. Therefore, we decided to use the maximum CT value for the vessel short axis as an index for assessing arterial enhancement. However, it is unrealistic in routine practice to make an LDP curve, or to measure the maximum CT value for the short axis at each site in the coronary artery. Therefore, using the maximum CT values for the descending aorta in the corresponding axial images as a substitute for the maximum CT values for the short axes of coronary arteries, and the abbreviated formula, $y=0.5x-75$, we developed an accurate and straightforward method for measuring the diameters of coronary arteries independent of arterial enhancement.

Acknowledgments

This work was supported by the Japan Cardiovascular Research Foundation, Takeda Science Foundation and GE Yokokawa Medical Systems.

References

1. Moshage WEL, Achenbach S, Seese B, Bachmann K, Kirchgeorg M. Coronary artery stenosis: Three-dimensional imaging with electrocardiographically triggered, contrast agent-enhanced, electron-beam CT. *Radiology* 1995; **196:** 707–714.
2. Achenbach S, Moshage W, Ropers D, Nossen J, Daniel WG. Value of electron-beam computed tomography for the noninvasive detection of high-grade coronary-artery stenoses and occlusions. *N Engl J Med* 1999; **339:** 1964–1971.
3. Budoff MJ, Oudiz RJ, Zalace CP, Bakhsheshi H, Goldberg SL, French WJ, et al. Intravenous three-dimensional coronary angiography using contrast enhanced electron beam computed tomography. *Am J Cardiol* 1999; **83:** 840–845.
4. Shimamoto R, Suzuki J, Nishikawa J, Fujimori Y, Nakamura F, Shin WS, et al. Measuring the diameter of coronary arteries on MR angiograms using spatial profile curves. *AJR Am J Roentgenol* 1998; **170:** 889–893.
5. Funabashi N, Rubin GD, Kobayashi Y, Shifrin RY, Wexler L, Perlroth M. Accuracy of coronary artery dimensions with electron-beam CT angiography: Comparison of measurement methods (abstract). *Radiology* 1999; **213(P):** 269.
6. Funabashi N, Kobayashi Y, Perlroth M, Rubin GD. Coronary artery; quantitative evaluation of normal artery diameter measurements determined by electron-beam computed tomography in comparison with cine coronary angiography: Initial experience. *Radiology* 2003; **226:** 263–271.
7. Pomerantsev EV, Kobayashi Y, Fitzgerald PJ, Grube E, Sanders WJ, Alderman EL, et al. Coronary stents: In vitro aspects of an angiographic and ultrasound quantification with in vivo correlation. *Circulation* 1998; **98:** 1495–1503.
8. Gould RG. Principles of ultrafast computed tomography: Historical aspects, mechanism of action, and scanner characteristics. *In*: Stanford W, Rumberger J, editors. Ultrafast computed tomography in cardiac imaging: Principles and practice. New York: Futura; 1992; 1–15.
9. Rumberger JA. Ultrafast computed tomography scanning modes, scanning planes and practical aspects of contrast administration. *In*: Stanford W, Rumberger J, editors. Ultrafast computed tomography in cardiac imaging: Principles and practice. New York: Futura; 1992; 17–24.
10. Chernoff DM, Ritchie CJ, Higgins CB. Evaluation of electron beam CT coronary angiography in healthy subjects. *AJR Am J Roentgenol* 1997; **169:** 93–99.
11. Funabashi N, Misumi K, Ohnishi H, Watanabe M, Suzuki Y, Imai N, et al. Endoluminal perspective volume rendering of coronary arteries using electron-beam computed tomography. *Circ J* 2003; **67:** 1064–1067.
12. Funabashi N, Matsumoto A, Yoshida T, Watanabe S, Misumi K, Masuda Y. Usefulness of three-dimensional visualization of coronary arteries using electron-beam computed tomography data with volume rendering. *Jpn Circ J* 2000; **64:** 644–646.
13. Funabashi N, Kobayashi Y, Rubin GD. Utility of three-dimensional volume rendering images using electron-beam computed tomography to evaluate possible causes of ischemia from an anomalous origin of the right coronary artery from the left sinus of Valsalva. *Jpn Circ J* 2001; **65:** 575–578.
14. Nakanishi T, Kohata M, Miyasaka K, Fukuoka H, Ito K, Imazu M. Virtual endoscopy of coronary arteries using contrast-enhanced ECG-triggered electron beam CT data sets. *AJR Am J Roentgenol* 2000; **174:** 1345–1347.
15. Achenbach S, Moshage W, Ropers D, Bachmann K. Comparison of vessel diameters in electron beam computed tomography and quantitative coronary angiography. *Int J Card Imaging* 1998; **14:** 1–7.
16. Ropers D, Baum U, Pohle K, Anders K, Ulzheimer S, Ohnesorge B, et al. Detection of coronary artery stenoses with thin-slice multi-detector row spiral computed tomography and multiplanar reconstruction. *Circulation* 2003; **107:** 664–666.
17. Sato Y, Kanmatsuse K, Inoue F, Horie T, Kato M, Kusama J, et al. Noninvasive coronary artery imaging by multislice spiral computed tomography. *Circ J* 2003; **67:** 107–111.
18. Fleischmann D, Rubin GD, Bankier AA, Hittmair K. Improved uniformity of aortic enhancement with customized contrast medium injection protocols at CT angiography. *Radiology* 2000; **214:** 363–371.

Available online at www.sciencedirect.com
SCIENCE DIRECT®
Biochemical and Biophysical Research Communications 322 (2004) 310–319
BBRC
www.elsevier.com/locate/ybbrc

Atrial natriuretic peptide inhibits cardiomyocyte hypertrophy through mitogen-activated protein kinase phosphatase-1

Doubun Hayashi[a,b], Sumiyo Kudoh[a], Ichiro Shiojima[a], Yunzeng Zou[d], Koichiro Harada[a], Masaki Shimoyama[a], Yasushi Imai[a], Koshiro Monzen[a,b], Tsutomu Yamazaki[a,c], Yoshio Yazaki[e], Ryozo Nagai[a], Issei Komuro[d,*]

[a] *Department of Cardiovascular Medicine, University of Tokyo Graduate School of Medicine, 7-3-1 Hongo, Bunkyo-ku, Tokyo 113-8655, Japan*
[b] *Department of Pharmacoepidemiology, University of Tokyo Graduate School of Medicine, 7-3-1 Hongo, Bunkyo-ku, Tokyo 113-8655, Japan*
[c] *Department of Clinical Bioinformatics, University of Tokyo Graduate School of Medicine, 7-3-1 Hongo, Bunkyo-ku, Tokyo 113-8655, Japan*
[d] *Department of Cardiovascular Science and Medicine, Chiba University Graduate School of Medicine, 1-8-1 Inohana, Chuo-ku, Chiba 260-8670, Japan*
[e] *International Medical Center of Japan, 1-21-1 Toyama, Shinjuku-ku, Tokyo 162-8655, Japan*

Received 5 June 2004

Abstract

Cardiac hypertrophy is formed in response to hemodynamic overload. Although a variety of factors such as catecholamines, angiotensin II (AngII), and endothelin-1 (ET-1) have been reported to induce cardiac hypertrophy, little is known regarding the factors that inhibit the development of cardiac hypertrophy. Production of atrial natriuretic peptide (ANP) is increased in the hypertrophied heart and ANP has recently been reported to inhibit the growth of various cell types. We therefore examined whether ANP inhibits the development of cardiac hypertrophy. Pretreatment of cultured cardiomyocytes with ANP inhibited the AngII- or ET-1-induced increase in the cell size and the protein synthesis. ANP also inhibited the AngII- or ET-1-induced hypertrophic responses such as activation of mitogen-activated protein kinase (MAPK) and induction of immediate early response genes and fetal type genes. To determine how ANP inhibits cardiomyocyte hypertrophy, we examined the mechanism of ANP-induced suppression of the MAPK activation. ANP strongly induced expression of MAPK phosphatase-1 (MKP-1) and overexpression of *MKP-1* inhibited AngII- or ET-1-induced hypertrophic responses. These growth-inhibitory actions of ANP were mimicked by a cyclic GMP analog 8-bromo-cyclic GMP. Taken together, ANP directly inhibits the growth factor-induced cardiomyocyte hypertrophy at least partly via induction of MKP-1. Our present study suggests that the formation of cardiac hypertrophy is regulated not only by positive but by negative factors in response to hemodynamic load.

Keywords: Angiotensin II; Atrial natriuretic peptide; Cardiac hypertrophy; Cardiomyocyte; Cyclic GMP; Endothelin-1; Growth factor; MAPK phosphatase-1; Mitogen-activated protein kinase; Vasoactive peptide

Since cardiac myocytes virtually lose their proliferative ability soon after birth, they respond to external stimuli not by increasing the cell number but by increasing the individual cell volume, called hypertrophy. Although cardiac hypertrophy has been considered to be a beneficial adaptive response of the heart to the increased workload, the hypertrophic heart often leads to dilated cardiomyopathy and eventually causes congestive heart failure after sustained overload [1]. Recent clinical studies have demonstrated that the increased ventricular mass is an independent risk factor for cardiac morbidity and mortality [2]. Therefore, it has become even more important to elucidate the molecular mechanism of how cardiac hypertrophy is formed.

* Corresponding author. Fax: +81 43 226 2557.
E-mail address: komuro-tky@umin.ac.jp (I. Komuro).

0006-291X/$ - see front matter © 2004 Elsevier Inc. All rights reserved.
doi:10.1016/j.bbrc.2004.07.119

A variety of factors have been implicated in the pathogenesis of cardiac hypertrophy [3]. Vasoactive peptides such as angiotensin II (AngII) [3–7] and endothelin-1 (ET-1) [8,9] have been reported to induce cardiomyocyte hypertrophy by autocrine or paracrine mechanisms. These factors are produced and secreted in the heart in response to the increased overload and induce cardiomyocyte hypertrophy. Antagonists of these factors effectively inhibit the load-induced cardiomyocyte hypertrophy [6–9]. The intracellular signaling pathways initiated by these growth factors and the resultant hypertrophic responses in cardiomyocytes have also been intensively investigated. AngII and ET-1 activate various protein kinases including protein kinase C and the mitogen-activated protein kinase (MAPK) family. Activation of these protein kinases induces expression of many specific genes [10–12] and an increase in protein synthesis [12].

Among the genes that are upregulated in the hypertrophied heart, atrial natriuretic peptide (ANP) has unique features. ANP reduces the hemodynamic load as a potent vasorelaxing and diuretic–natriuretic peptide, which indirectly inhibits the development of cardiac hypertrophy [13]. In addition to the indirect effects of ANP via hemodynamics, ANP has recently been reported to have direct growth-inhibitory effects in various cell types such as vascular smooth muscle cells, glomerular mesangial cells, endothelial cells, cardiac fibroblasts, and astrocytes [14–19]. In these cells, 8-bromo-cyclic GMP (8-Br-cGMP), a cell permeable analog of cyclic GMP (cGMP), mimicked the effects of ANP, indicating that the growth-inhibitory effects of ANP are dependent on cGMP. Furthermore, it has recently been reported that ANP induces expression of MAPK phosphatase-1 (MKP-1) [20]. MKP-1 is a dual serine/threonine and tyrosine phosphatase and specifically inactivates MAPK family members [21]. Overexpression of MKP-1 blocks the MAPK-dependent gene expression and inhibits cell proliferation [22–24]. These observations suggest that ANP may exert its inhibitory effects on cell growth through inactivation of MAPK family members by induction of MKP-1. Three members of the MAPK family, the extracellular signal-regulated kinases (ERKs), the c-Jun NH_2-terminal kinases/stress-activated protein kinases (JNKs/SAPKs), and p38MAPKs, have been shown to be activated by hypertrophic stimuli in cardiac myocytes and have been implicated in the development of cardiac hypertrophy [25–30].

In the present study, we examined whether ANP has direct inhibitory effects on growth factor-induced cardiomyocyte hypertrophy. Pretreatment with ANP suppressed the growth factor-induced increase in the cell volume and the protein synthesis of cardiomyocytes. ANP also inhibited hypertrophic responses such as activation of MAPK and induction of immediate early response genes and fetal type genes. In addition, ANP strongly induced expression of MKP-1 in cardiac myocytes and overexpression of *MKP-1* suppressed AngII-induced gene expressions. These results suggest that anti-hypertrophic effects of ANP are, at least in part, mediated by inactivation of MAPK via induction of MKP-1. These inhibitory actions of ANP were mimicked by a cGMP analog, 8-Br-cGMP.

Materials and methods

Reagents. [γ-^{32}P]ATP and [^{3}H]phenylalanine were purchased from Du Point-New England Nuclear. Dulbecco's modified Eagle's medium (DMEM) and fetal bovine serum (FBS) were from Gibco-BRL. Polyclonal antibodies against MKP-1 were purchased from Santa Cruz Biotechnology. A rat ANP [1–28], AngII, myelin basic protein (MBP), and other reagents were purchased from Sigma.

Cell culture. Primary cultures of cardiomyocytes were prepared from ventricles of 1-day-old Wistar rats as described previously [6]. Except for the reporter gene assay, cells were plated at a field density of 1×10^3 cells/mm^2 on 35-mm culture dishes and cultured in DMEM with 10% FBS for the first 24 h, and then the culture medium was changed to DMEM containing 0.1% FBS. After 48 h of serum starvation, cardiomyocytes were stimulated by various agents. For transfection and reporter gene assay, cells were plated at the same density, and subjected to transfection after 24 h of culture in DMEM with 10% FBS.

Immunofluorescence. Immunostaining of cardiomyocytes with MF20, a monoclonal antibody against sarcomeric myosin heavy chain (MHC), was performed as described previously [7]. An anti-mouse immunoglobulin G conjugated with tetramethyl rhodamine isothiocyanate was used as the secondary antibody. The cell size of cardiomyocytes was measured by directly tracing the stained areas on a photograph.

[^{3}H]Phenylalanine incorporation. Protein synthesis was assessed by measuring the [^{3}H]phenylalanine incorporation as previously described [7]. Cardiac myocytes were cultured for 2 days without serum and then incubated for 24 h with AngII, ET-1 or vehicle. [^{3}H]Phenylalanine (1.0 μCi/ml) was added 3 h before the harvest. Cells were washed three times with ice-cold phosphate-buffered saline (PBS), incubated 30 min with 1 ml of 10% trichloroacetic acid, and washed twice with PBS. Precipitates were solubilized for 30 min in 800 μl of 1 N NaOH, and radioactivity was measured by liquid scintillation spectroscopy.

Northern blot analysis. Total cellular RNA was extracted from cardiac myocytes by acid-guanidine phenol–chloroform method. Ten micrograms of total RNA was size-fractionated by 1.2% agarose gels and transferred to nylon membranes. Northern blot analyses were performed using the *c-fos* and *ANP* cDNA as probes as described previously [26,31]. The cDNA of rat *MKP-1* was isolated by the polymerase chain reaction method with a pair of primers corresponding to the amino acids 174–181 and 342–349.

Transfection and reporter gene assay. The luciferase reporter plasmids (3 μg/dish) containing ~1800 bp 5′ flanking region of the *brain natriuretic peptide* (*BNP*) gene (a kind gift from Dr. Y. Saito, Kyoto) were transiently transfected into cultured cardiac myocytes using standard calcium phosphate method. Cells were washed with PBS at 12 h after transfection and culture medium was changed to the medium containing 0.1% FBS. After 24 h of serum starvation, cells were treated with various reagents. Cells were harvested at 48 h after stimulation in 150 μl of extraction buffer (100 mM tricine, 10 mM $MgSO_4$, 2 mM EDTA, pH 7.8, and 1 mM dithiothreitol) and luciferase activities were measured by Berthold Lumat LB9501 luminometer. Next, 1 μg of luciferase reporter plasmids containing the human *c-fos* promoter

(pFC2) [32] or rat β *myosin heavy chain* (*βMHC*) promoter (−354 to +33) [33] and 3 μg of *MKP-1* expression plasmid DNA were co-transfected into cultured cardiac myocytes using lipofectin, Tfx-50 (Promega, WI, USA), according to the manufacturer's instructions. At 4 h after the transfection, the culture medium was changed to 0.1% FCS-containing DMEM and 24 h later, cardiac myocytes were exposed to 10^{-6} M Ang II for 4 h. Differences in transfection efficiency were corrected by β-galactosidase activities of co-transfected *SV40-βgal* plasmids (0.5 μg/dish).

Immunoprecipitation and Western blot analysis. Cardiomyocytes were lysed with lysis buffer (1% Triton X-100, 50 mM Tris–HCl, pH 7.6, 150 mM NaCl, 100 μM sodium orthovanadate, 1 mM EDTA, 1 mM phenylmethylsulfonyl fluoride PMSF, and 1 mM aprotinin) and protein extract was immunoprecipitated with a polyclonal anti-MKP-1 antibody. Immunoprecipitates were subjected to SDS–PAGE and immunoblotted with the same anti-MKP-1 antibody. The anti-rabbit IgG conjugated with horseradish peroxidase was used as the secondary antibody and immune complexes were visualized using the ECL detection kit according to the manufacturer's directions.

Assay of ERK activity. The activity of ERKs was examined by "in gel assay" using MBP-containing gel as described previously [7]. In brief, cells were lysed with 100 ml Buffer A (25 mM Tris–HCl, pH 7.4, 25 mM NaCl, 1 mM sodium orthovanadate, 10 mM NaF, 10 mM sodium pyrophosphate, 10 nM okadaic acid, 0.5 mM EGTA, and 1 mM PMSF) and 25 μl of cell lysates was applied to an SDS–polyacrylamide gel containing 0.5 mg/ml MBP. ERKs in the gel were denatured in 6 M guanidine-HCl and renatured in 50 mM Tris–HCl, pH 8.0, containing 0.04% Triton X-100, and 5 mM of 2-mercaptoethanol. The activity of ERKs was assayed by incubating the gel with [γ-^{32}P]ATP. After incubation, the gel was washed, dried, and subjected to autoradiography.

Statistical analysis. All results are expressed as means ± SEM. One-way ANOVA and Fisher's exact test for post hoc analyses carried out multiple comparisons among three or more groups. A value of $P < 0.05$ was considered statistically significant.

Results

ANP inhibited AngII- or ET-1-induced cardiomyocyte hypertrophy

To examine whether ANP directly inhibits the development of cardiomyocyte hypertrophy, cultured cardiomyocytes were pretreated with ANP and then stimulated by AngII or ET-1. AngII or ET-1 enhanced the cell size of cardiomyocytes by approximately 2.6- or 3.2-fold, respectively (Figs. 1A and B). Pretreatment of cardiomyocytes with ANP (10^{-7} M) for 2 h significantly inhibited the AngII- or ET-1-induced increase in the cell size (Figs. 1A and B). A cGMP analog 8-Br-cGMP (10^{-3} M) also significantly blocked the vasoactive peptide-induced increase in the cell size (Fig. 1B). We also examined the protein synthesis in cardiomyocytes which were pretreated with ANP and subsequently stimulated by the vasoactive peptides. AngII or ET-1 stimulation increased the phenylalanine incorporation in cardiomyocytes by approximately 1.5- or 1.8-fold, respectively (Fig. 1C), which is consistent with previous results [5,7,9]. Pretreatment with ANP significantly reduced the AngII- or ET-1-induced increase in phenylalanine incorporation (Fig. 1C). 8-Br-cGMP also significantly inhibited the vasoactive peptide-induced phenylalanine incorporation (Fig. 1C). To confirm the relationship between ANP and cGMP in cardiomyocytes, we examined the concentrations of cGMP in the culture media after treatment of cardiomyocytes with ANP. The ANP treatment increased the cGMP concentrations in a dose-dependent manner, suggesting that ANP induces the cGMP generation, and secretion from cardiomyocytes (Fig. 1D). Furthermore, we investigated whether changes in the cGMP activity influence the inhibitory actions of ANP on vasoactive peptide-induced hypertrophic responses. Pretreatment with a selective inhibitor of the cGMP-specific phosphodiesterase (ZAPRINAST), which increases the cGMP concentration by blocking its metabolism, enhanced the inhibitory effect of ANP on AngII- or ET-1- induced increase in phenylalanine incorporation (Fig. 1E). On the other hand, pretreatment with a cGMP-dependent protein kinase inhibitor (KT5823), which blocks signals from cGMP, suppressed it (Fig. 1E). These effects of ZAPRINAST or KT5823 on actions of ANP were statistically significant in case of ET-1, though not of Ang II (Fig. 1E). These results suggest that ANP has a direct inhibitory effect on vasoactive peptide-induced cardiomyocyte hypertrophy in a cGMP-dependent manner.

ANP inhibited AngII- or ET-1-induced hypertrophic responses in cardiomyocytes

We next examined the effects of ANP on AngII- or ET-1-induced hypertrophic responses such as specific gene expressions. AngII induced expression of the *c-fos* gene in cardiac myocytes and the induction was inhibited by the pretreatment with 10^{-7} M ANP (Fig. 2A). The inhibitory effect of ANP on the *c-fos* gene induction was mimicked by the pretreatment with 10^{-3} M 8-Br-cGMP (Fig. 2A). We also examined the effects of ANP on the induction of fetal cardiac genes by AngII or ET-1. Both AngII and ET-1 increased the expression levels of the *ANP* gene, and pretreatment with ANP or 8-Br-cGMP inhibited AngII- or ET-1-induced increase in the *ANP* mRNA levels (Fig. 2B). To elucidate whether ANP inhibits the induction of fetal genes at the transcriptional level, we examined the effects of ANP on the *BNP* promoter activity. AngII or ET-1 activated the *BNP* promoter by approximately 2.5- or 3.5-fold, respectively (Fig. 2C). This transcriptional activation was significantly inhibited by the pretreatment of cardiomyocytes with ANP (10^{-7} M) or 8-Br-cGMP (10^{-3} M), although ANP or 8-Br-cGMP had no effects on the basal promoter activity of *BNP* (Fig. 2C). These results suggest that ANP inhibits the vasoactive peptide-induced reprogramming of gene expression in cardiomyocytes in a cGMP-dependent manner.

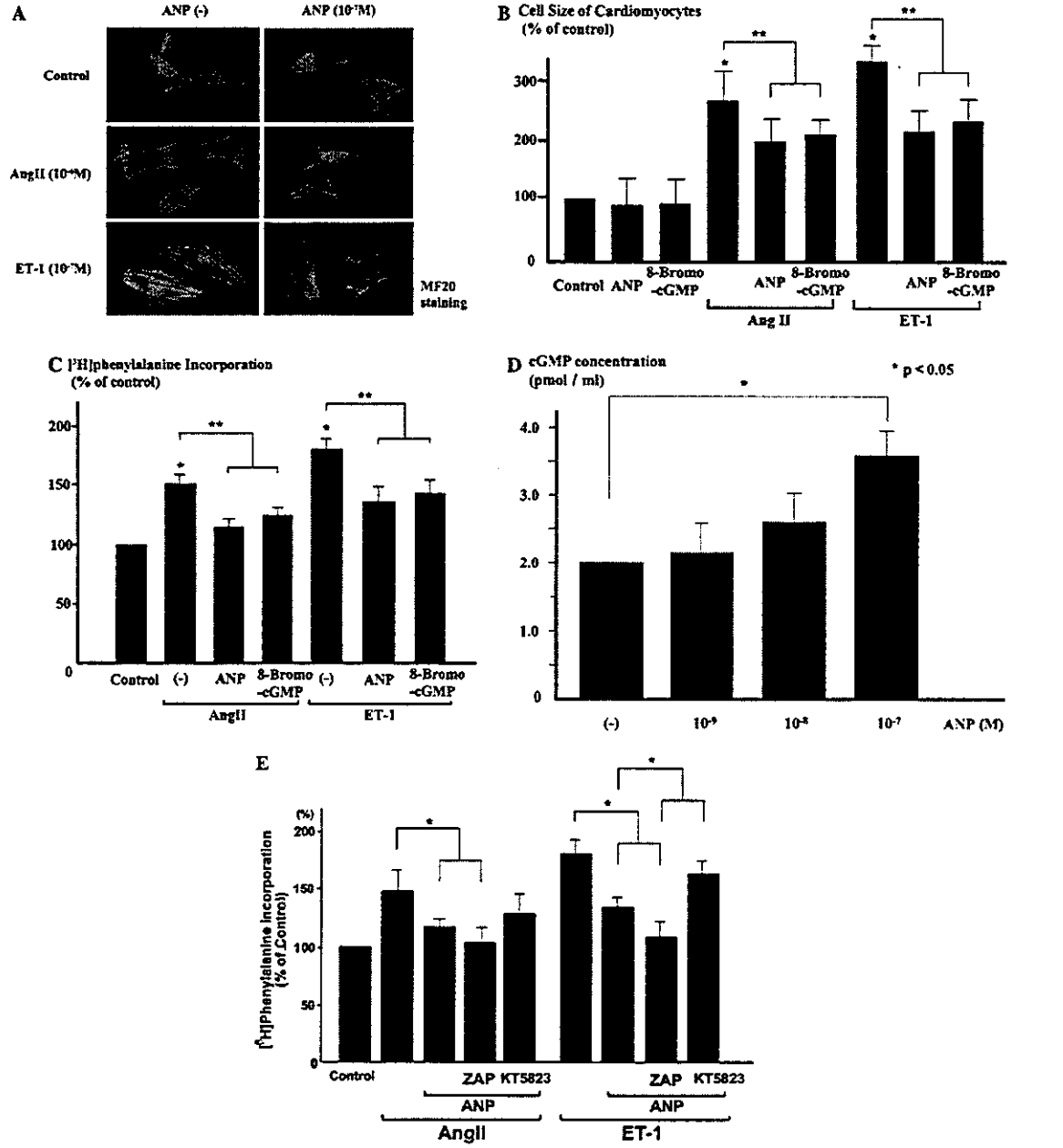

Fig. 1. ANP inhibited AngII- or ET-1-induced increase in the cell size and the protein synthesis of cardiomyocytes. (A,B) After pretreatment with ANP (10^{-7} M) or 8-Br-cGMP (10^{-3} M) for 2h, cultured cardiomyocytes were stimulated with 10^{-6} M AngII or 10^{-7} M ET-1 for 24h and then the cells were immunostained with MF20, an anti-sarcomeric MHC antibody, 24h later. The cell size of cardiomyocytes was measured by directly tracing the stained areas on a photograph. Data represent the average percentages against the control (=100%, vehicle) from three independent experiments (mean ± SE). Statistical differences ($P < 0.05$) between the non-treated control and the Ang II or ET-1 treatment are denoted by *, and those between no pretreatment and ANP or 8-Br-cGMP pretreatment are shown by **. (C) After pretreatment with ANP (10^{-7} M) or 8-Br-cGMP (10^{-3} M) for 2h and subsequent stimulation with AngII (10^{-6} M) or ET-1 (10^{-7} M) for 24h, [^{3}H]phenylalanine (1 μCi/ml) was added 3h before harvest. The effects of ANP or 8-Br-cGMP on the protein synthesis were evaluated by measuring the [^{3}H]phenylalanine incorporation. The total radioactivity of incorporated [^{3}H]phenylalanine was determined by liquid scintillation counting. Data represent the average percentages against the control (=100%, vehicle) from three independent experiments (means ± SE). Statistical differences ($P < 0.05$) between the non-treated control and the AngII or ET-1 treatment are denoted by *, and those between no pretreatment and ANP or 8-Br-cGMP pretreatment are shown by **. (D) After serum starvation of cultured cardiomyocytes with 0.1% FBS for 48h and subsequent treatment with ANP at indicated concentrations for 24h, the concentrations of cGMP in the culture media were examined. Statistical differences ($P < 0.05$) from the non-treated control are denoted by *. (E) After pretreatment with ANP (10^{-7} M) along with ZAPRINAST (ZAP) and KT5823 (10^{-8} M each) for 2h and subsequent stimulation with AngII (10^{-6} M) or ET-1 (10^{-7} M) for 24h, [^{3}H]phenylalanine (1 μCi/ml) was added 3h before harvest. The evaluation of the [^{3}H]phenylalanine incorporation is similar to that in (C).

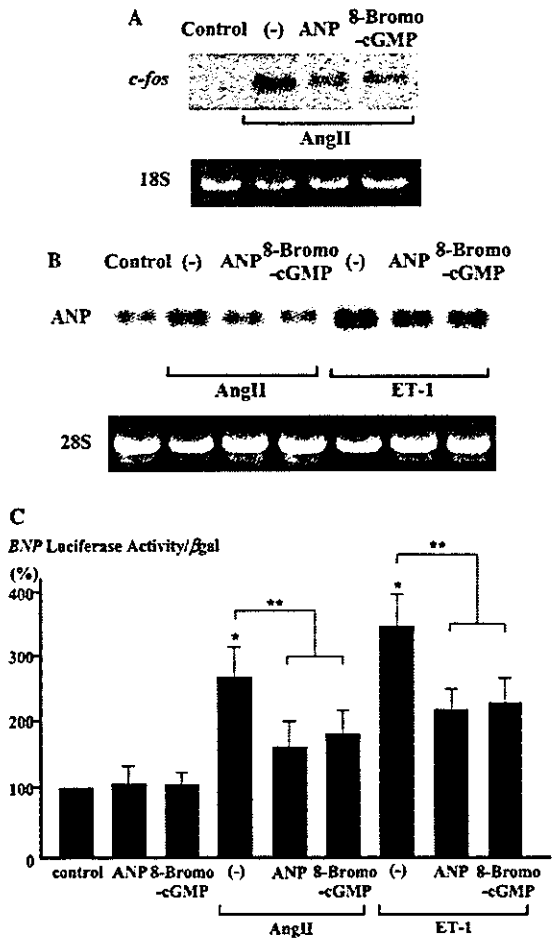

Fig. 2. ANP inhibited AngII- or ET-1-induced hypertrophic responses in cardiomyocytes. (A) Expression of the *c-fos* gene was examined by Northern blot analysis. Cardiomyocytes were pretreated for 2h with ANP (10^{-7}M) or 8-Br-cGMP (10^{-3}M) and stimulated with AngII (10^{-6}M) for 30min. A representative autoradiogram is shown. (B) The *ANP* gene expression was examined by Northern blot analysis. Cardiomyocytes were pretreated for 24h with ANP (10^{-7}M) or 8-Br-cGMP (10^{-3}M) and stimulated with AngII (10^{-6}M) or ET-1 (10^{-7}M) for 2h. A representative autoradiogram is shown. (C) The *BNP* promoter activity was examined by transient transfection assay. The results are indicated as means ± SEM of three independent experiments ($n = 9$) compared with unstimulated controls (100%). Statistical differences ($P < 0.05$) between the non-treated control and the AngII or ET-1 treatment are denoted by *, and those between no pretreatment and the ANP or 8-Br-cGMP pretreatment are shown by **.

ANP decreased basal activities of ERKs in cardiomyocytes in a cGMP-dependent manner

We next examined the effects of ANP on MAPK, which has been reported to be important for the induction of cardiac hypertrophy [10,11]. The in-gel assay revealed that basal activities of both 44kDa (ERK1) and 42kDa (ERK2) ERKs were reduced by the treatment with ANP in a dose-dependent manner (Fig. 3A) and a significant decrease in ERK activities was observed at 60min and reached the minimum level at 120min after the 10^{-7}M ANP treatment (Fig. 3B). 8-Br-cGMP decreased basal activities of ERKs in a dose-dependent manner (Fig. 3C) with the same time course as ANP (Fig. 3D). These results suggest that ANP represses the basal ERK activity in a cGMP-dependent manner in cardiac myocytes.

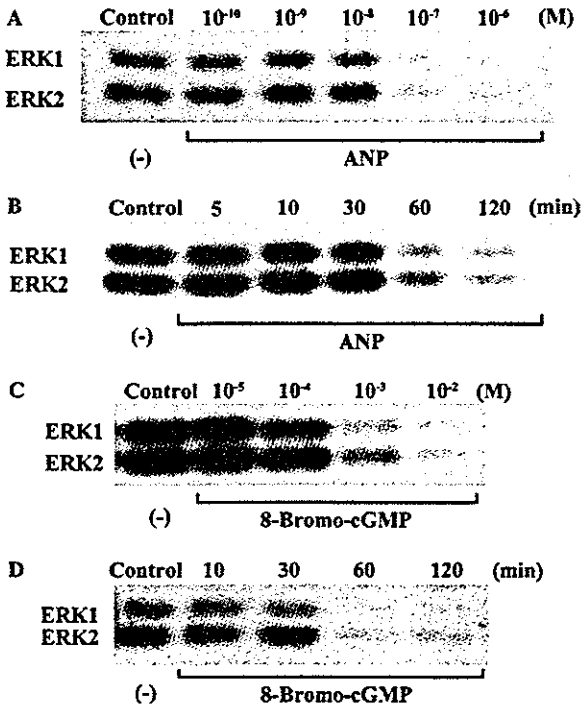

Fig. 3. ANP suppressed basal activities of ERKs in cardiomyocytes. (A) Cultured cardiomyocytes were treated with various concentrations of ANP (10^{-10}–10^{-6}M) for 2h and the activities of ERKs were measured by the in-gel kinase assay described in "Materials and methods." (B) Cultured cardiomyocytes were treated with 10^{-7}M ANP and ERK activities were examined for indicated periods of time. (C) Cultured cardiomyocytes were treated with various concentrations of 8-Br-cGMP (10^{-5}–10^{-2}M) for 2h and the activities of ERKs were measured. (D) Cultured cardiomyocytes were treated with 8-Br-cGMP (10^{-3}M) and ERK activities were examined for indicated periods of time. Representative autoradiograms are shown.

ANP inhibited vasoactive peptide-induced activation of MAPKs in a cGMP-dependent manner

We next examined whether ANP represses the vasoactive peptide-induced activation of MAPK. Treatment of cardiomyocytes with 10^{-6}M AngII or 10^{-7}M ET-1 for 10min markedly increased the ERK activity as reported before [7,9]. This vasoactive peptide-induced increase in the ERK activity was significantly inhibited by the pretreatment with 10^{-7}M

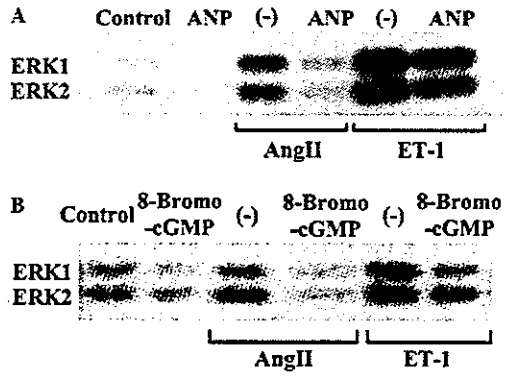

Fig. 4. ANP inhibited AngII- or ET-1-induced activation of MAPK in cardiomyocytes. (A) Cultured cardiomyocytes were pretreated with ANP (10^{-7}M) for 2h and stimulated with AngII or ET-1 for 10min. ERK activities were measured by the in-gel kinase assay. (B) Cultured cardiomyocytes were stimulated with AngII or ET-1 for 10min and the effects of 8-Br-cGMP (10^{-3}M) pretreatment for 2h on ERK activities were examined by the in-gel kinase assay. Representative autoradiograms are shown.

ANP for 2h (Fig. 4A). The effects of 8-Br-cGMP on vasoactive peptide-induced ERK activation were also examined. Pretreatment of cardiomyocytes with 10^{-3}M 8-Br-cGMP decreased the AngII- or ET-1-induced ERK activation by approximately 70% and 60%, respectively (Fig. 4B).

ANP induced MKP-1 expression in cardiomyocytes

MAPK is inactivated by a dual phosphatase, MKP-1 [21], and the induction of MKP-1 has been implicated in the growth-inhibitory effects of ANP in mesangial cells [20]. To elucidate the mechanism by which ANP inhibits the development of cardiomyocyte hypertrophy, we examined whether MKP-1 is induced in cardiomyocytes by ANP. ANP significantly increased expression levels of the *MKP-1* gene and the mRNA levels of *MKP-1* peaked at 30min and returned to the basal level at 120min after the treatment with ANP (10^{-7}M) (Fig. 5A). 8-Br-cGMP (10^{-3}M) also induced MKP-1 by the same time course (Fig. 5A). The protein content of MKP-1 was also examined by Western blot analysis. The MKP-1 protein was dramatically induced by ANP or 8-Br-cGMP with its peak at 120min after the treatment (Fig. 5B). These results clearly indicate that ANP induces expression of MKP-1 in cardiomyocytes in a cGMP-dependent manner.

MKP-1 blocked vasoactive peptide-induced hypertrophic responses

To elucidate the significance of the increase in the *MKP-1* gene expression, we examined the effects of

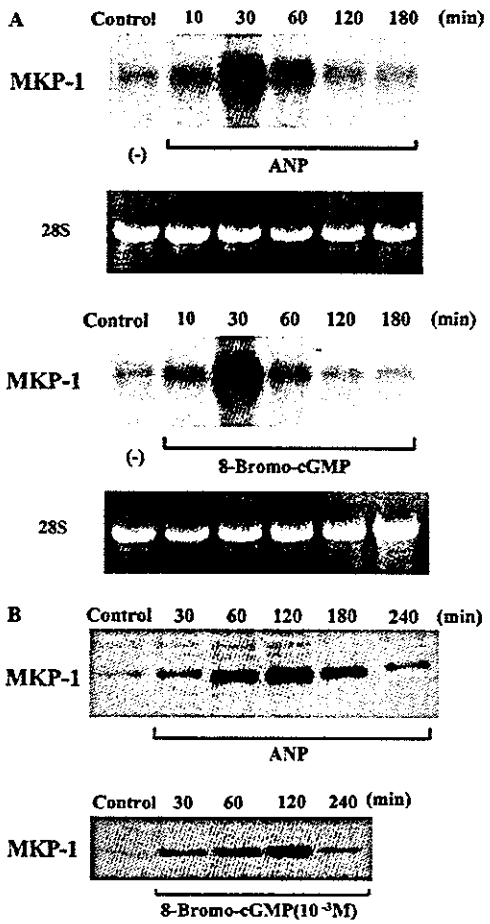

Fig. 5. ANP induced expression of MKP-1 in cardiomyocytes. (A) Cultured cardiomyocytes were treated with ANP or 8-Br-cGMP for indicated periods of time and expression of the *MKP-1* mRNA was examined by Northern blot analysis. (B) Cultured cardiomyocytes were treated with ANP or 8-Br-cGMP for the indicated periods of time and the protein content of MKP-1 was examined by immunoblot analysis. Representative autoradiograms are shown.

overexpression of the *MKP-1* gene on hypertrophic responses such as induction of the *c-fos* and *βMHC* genes. We co-transfected *c-fos* or *βMHC* promoter-containing luciferase reporter plasmids and *MKP-1* expression plasmids into the cultured cardiomyocytes, and examined the luciferase activity after stimulation with AngII. AngII activated the *c-fos* gene transcription in cardiomyocytes (Fig. 6A). Overexpression of the *MKP-1* mRNA significantly suppressed the AngII-induced increase in the *c-fos* gene transcription as well as the non-treated, basal transcription (Fig. 6A). AngII also increased the luciferase activity of the *βMHC* reporter gene and overexpression of *MKP-1* significantly suppressed the AngII-induced increase in the *βMHC* gene transcription (Fig. 6B). Furthermore, overexpression of *MKP-1* significantly suppressed AngII- or ET-1-induced increase in

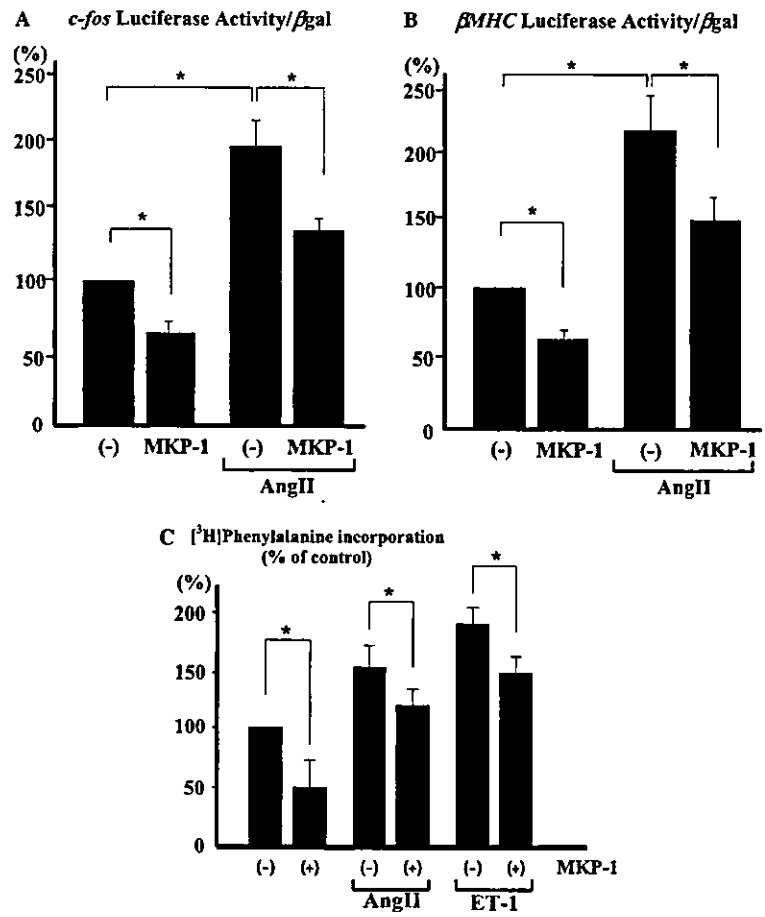

Fig. 6. MKP-1 blocked AngII- or ET-1-induced hypertrophic responses in cardiomyocytes. (A,B) One microgram of MKP-1 plasmid DNA was co-transfected with 1 μg of *c-fos* (A) or *βMHC* (B) luciferase reporter plasmids into cultured cardiomyocytes using lipofectin, Tfx-50. At 4 h after the transfection, the culture medium was changed to 0.1% FBS-containing DMEM. After this serum starvation for 24 h, cardiomyocytes were incubated with Ang II (10^{-6} M) for 4 h. Luciferase activities were measured using a luminometer and the data are shown as means ± SEM of three independent assays ($n = 18$) ($^*P < 0.05$). (C) After the transfection and the starvation same as those in (A,B), cardiomyocytes were incubated with Ang II (10^{-6} M) and ET-1 (10^{-7} M) for 24 h. [^{3}H]Phenylalanine (1 μCi/ml) was added 3 h before harvest. The evaluation of the [^{3}H]phenylalanine incorporation is similar to that in Fig. 1C. Statistical differences ($P < 0.05$) from the non-transfected control are denoted by *.

phenylalanine incorporation (Fig. 6C). These findings suggest that an increase in the *MKP-1* mRNA levels inhibits vasoactive peptide-induced hypertrophic responses such as an increase in protein synthesis and specific gene expressions.

Discussion

In the present study, we have obtained several results as follows. (i) ANP directly inhibits the vasoactive peptide-induced increase in the cell size and the protein synthesis of cardiomyocytes through the cGMP-dependent pathway. (ii) ANP also inhibits the vasoactive peptide-induced hypertrophic responses such as reprogramming of gene expressions and activation of MAPK. (iii) ANP upregulates expression of MKP-1 in cardiomyocytes. (iv) Overexpression of *MKP-1* inhibits the vasoactive peptide-induced hypertrophic responses.

ANP was originally identified as a natriuretic and diuretic peptide predominantly produced and secreted from atrial cells. Many studies demonstrated that ANP regulates sodium and water homeostasis via changes in the glomerular filtration rate and inhibition of the renin and aldosterone secretion [13]. In addition to these effects on the circulatory system, ANP has been shown to have a direct vasorelaxing effect which counteracts the vasoconstrictive factors such as AngII and ET-1 [13]. Moreover, it has recently been demonstrated that ANP acts as a growth-inhibitory factor that antagonizes the growth-promoting effects of AngII or ET-1 in various cell types including vascular smooth muscle

cells, glomerular mesangial cells, astrocytes, endothelial cells, and cardiac fibloblasts [14–19]. These findings suggest that ANP antagonizes various effects of vasoactive and/or growth-promoting factors. We therefore hypothesized that ANP might antagonize cardiomyocyte hypertrophy-promoting effects of vasoactive peptides. In the present study, in fact, ANP inhibited the AngII- or ET-1-induced increase in protein synthesis and hypertrophic responses such as expression of *c-fos* and fetal type genes and activation of MAPK in cardiomyocytes.

ANP and the other natriuretic peptides function through a family of membrane receptors called natriuretic peptide receptors, NPR-A, NPR-B, and NPR-C [13]. NPR-A and NPR-B have three domains, an extracellular ligand-binding domain, a single transmembrane domain, and an intracellular domain. An intracellular domain is consisting of a kinase domain and a guanylyl cyclase domain, which generates cGMP upon ligand binding [13]. On the other hand, NPR-C or clearance receptor contains the extracellular and transmembrane domains but lacks the intracellular domain, and is thought to be mainly responsible for the internalization and degradation of ligands [13]. Our present data strongly suggest that the anti-hypertrophic actions of ANP are mediated by guanylyl cyclase-linked NPR-A because a cGMP analog 8-Br-cGMP showed the effects similar to ANP and also because ANP exhibits relatively higher binding affinity for NPR-A than for NPR-B. Another recent report demonstrated that the inhibitory action of ANP on hypertrophic response was not suppressed by a cGMP-dependent protein kinase inhibitor KT5823, implying the involvement of additional cGMP-independent pathways [34]. This result and our present results are controversial, which may be at least partially due to differences in cardiomyocytes used in assays (adult vs. neonatal) and the ways how to stimulate them (concentration, duration, etc.). Nevertheless, we consider our data clearly and for the first time demonstrated a series of evidence that the cGMP analog mimicked the effects of ANP on vasoactive peptide-induced cardiomyocyte hypertrophy, indicating the importance of the cGMP-dependent pathway for this anti-hypertrophic action of ANP. The growth-inhibitory effects of ANP on glomerular mesangial cells [20] and vascular smooth muscle cells [18] are also thought to be mediated by cGMP-dependent pathways, although the anti-proliferative actions of ANP on astrocytes [19] are reported to be mediated by clearance receptors, suggesting that modes of inhibitory actions of ANP may depend on cell types nonetheless.

Although the mechanism by which AngII or ET-1 induces cardiomyocyte hypertrophy is not fully understood, protein kinases especially the MAPK family have been reported to play a pivotal role in the development of cardiac hypertrophy [10,11,27–30]. Three subfamilies of MAPKs such as ERKs, JNK, and p38MAPK have been reported to be involved in cardiac hypertrophy as follows. (i) Hypertrophic stimuli such as AngII and ET-1 activate all three members of MAPKs [5–7,9,26,29]. (ii) Anti-sense oligonucleotides against ERKs inhibit the phenylephrine-induced increase in cell size [12]. (iii) Selective activation of JNK by a constitutively active form of MKK7/JNKK2 leads to cardiomyocyte hypertrophy [30]. (iv) Activation of p38MAPK induces cardiomyocyte hypertrophy while that of JNK exhibits inhibitory effects [27]. (v) p38MAPK is necessary for the maintenance of hypertrophic response in a longer period but not for the immediate morphological responses [29]. Taken together, although precise roles of individual MAPKs are still controversial at present, these results suggest that activation of the MAPK pathways plays a critical role in the development of cardiomyocyte hypertrophy. In this respect, MKP-1, the recently identified dual protein phosphatase with selectivity for MAPKs, is of quite interest as a negative regulator of the MAPK pathways [21]. MKP-1 has been shown to be widely expressed in various cell types and to be capable of dephosphorylating phosphothreonine and phosphotyrosine residues of ERKs, JNK, and p38MAPK [21,24,32]. Because expression of MKP-1 is rapidly induced by many growth factors and cytokines that also induce activation of ERKs, JNK, and p38MAPK, MKP-1 has been implicated for the feedback loop serving to downregulate the MAPK activities in response to external stimuli [21,24,32]. Recently, MKP-1 has been reported to be induced by ANP in glomerular mesangial cells [20]. MKP-1 was also induced by ANP in cardiomyocytes in this study, although ANP did not activate ERKs in cardiomyocytes (data not shown). ANP also reduced the basal MAPK activity and inhibited vasoactive peptide-induced activation of MAPK in cardiomyocytes through the cGMP-dependent pathways. Taken together, our present study suggests that ANP inhibits the vasoactive peptide-induced cardiomyocyte hypertrophy at least in part by inhibiting activation of MAPK through upregulation of MKP-1.

In addition to the induction of MKP-1, there are possible mechanisms by which ANP inhibits the growth-promoting processes in various cell types. In astrocytes, ANP has been shown to inhibit ERKs by attenuating the MEK activity, although the precise signaling pathway leading to the inactivation of MEK remains to be identified [19]. In mesangial cells, ANP inhibits the ET-1-induced JNK activation possibly by attenuating the ET-1-induced increase in intracellular Ca^{2+} concentration [33]. It has been reported that ANP inhibits the norepinephrine-induced growth of cardiac myocytes by a cGMP-mediated inhibition of norepinephrine-stimulated Ca^{2+} influx [35]. Although MKP-1 was strongly induced in cardiomyocytes by ANP, we cannot rule out